Material removal and surface generation in longitudinal-torsional ultrasonic assisted milling

Shaoqing Qin[a1], Lida Zhu[a1*], Marian Wiercigroch[b*], Tianyu Ren[a], Yanpeng Hao[a], Jinsheng Ning[a], Jinze Zhao[a]

[a]School of Mechanical Engineering and Automation, Northeastern University, Shenyang, 110819, China

[b]Centre for Applied Dynamics Research, School of Engineering, University of Aberdeen, Scotland, UK

[1]Co-first Author; *Corresponding author, e-mail addresses: neulidazhu@163.com, m.wiercigroch@abdn.ac.uk

Abstract: Ultrasonic Machining (UM) is extensively used in processing of difficult to cut materials due to its superior performance. However, the mechanics of this process is still not fully understood when superimposed on other machining operations. In this paper, Longitudinal-Torsional Ultrasonic Assisted Milling (LTUAM) is introduced for machining of a high strength titanium alloy Ti-6Al-4V. The separation geometrical characteristics between the tool and workpiece are studied analytically. Moreover, the texturing generation mechanism of LTUAM is firstly analyzed through a theoretical model. The proposed method considers the influence of 3D tool topography, which can accurately simulate the ultrasonic surface topography. Related experiments of the generated cutting force and the surface topography were conducted to investigate the machining characteristics. The results showed that compared with Conventional Milling (CM), a noticeable decrease of the cutting force was observed in LTUAM. This can be explained from the perspective of tool workpiece contact rate model. Micro dimpled surface textures were successfully fabricated on Ti-Al6-4V using LTUAM technique. The surface test results indicated that the surface micro-hardness was enhanced between 6.34% and 13.22% compared with CM. This research provides guidance for the application of ultrasonic machining of textured surfaces.

Keywords: Longitudinal-torsional ultrasonic assisted milling; Material removal process; Cutting force; Micro dimpled textures; Surface micro-hardness.

Nomenclature

CM	conventional milling	UM	ultrasonic machining
LTUAM	longitudinal-torsional ultrasonic assisted milling		
R	tool radius(mm)	v_f	feed velocity (mm/min)
β	tool helix angle (°)	α	clearance angle of the tool (rad)
κ	angle of the secondary cutting edge of the tool (rad)	f_z	feed per tooth(mm/Z)
t_s	separation time at each ultrasonic vibration cycle (s)	r	tool-workpiece contact rate
w_r	tool rotation angular velocity (rad/s)	T	ultrasonic vibration period

			(s)
N	number of tool teeth	h	height of the ridge(μm)
$X_\mathrm{w}Y_\mathrm{w}Z_\mathrm{w}$	workpiece coordinate system	$X_\mathrm{f}Y_\mathrm{f}Z_\mathrm{f}$	feed coordinate system
$X_\mathrm{t}Y_\mathrm{t}Z_\mathrm{t}$	tool coordinate system	$O_1X_1Z_1$	coordinate system expanded along the cutting direction
$t_\mathrm{A}, t_\mathrm{D}$	start and end moments at each ultrasonic cycle (s)		
$\theta_\mathrm{m,n}, r_\mathrm{m,n}$	the radian and radius at position (m, n)		
(x_0, y_0, z_0)	initial position O_f of feed coordinate system with point O_w of workpiece coordinate system		
$(x_w(t), y_w($	tool tip kinematic trajectories in $X_\mathrm{w}Y_\mathrm{w}Z_\mathrm{w}$		
$(x_t(t), y_t(t$	tool tip kinematic trajectories in $X_tY_tZ_t$		
$(x_t(t), z_t(t$	tool tip kinematic trajectories in $O_1X_1Z_1$		
$(x_{m,n}, y_{m,n},$	discrete coordinate points of the tool cutting edge in $X_tY_tZ_t$		
$l_\mathrm{m,n}$	arc length that the tool is expanded in the circumferential direction		
$\theta_\mathrm{m,n}, r_\mathrm{m,n}$	radian and radius at position (m,n)		
A,B	amplitudes of longitudinal and torsional ultrasonic vibration (μm)		
φ_1, φ_2	initial phase of longitudinal and torsional vibration (rad)		
w_f	ultrasonic vibration angular velocity (rad/s)		
$V_\mathrm{t}, V_\mathrm{h}$	cutting velocity along the cutting edge and perpendicular to the cutting edge (mm/s)		
v_a, v_r	ultrasonic velocity of longitudinal and torsional vibration (mm/s)		
v_c	cutting velocity of the tool (mm/s)		
λ_1	ratio of the ultrasonic frequency to the spindle rotation velocity		
λ_2	ratio of the ultrasonic frequency to the tool tooth frequency		
d	distance between two adjacent dimples along the cutting velocity (μm)		
δ_1	phase shift distance of the adjacent dimples between the single tooth(rad)		
δ_2	phase shift distance of the adjacent dimples between the adjacent tooth(rad)		
η	maximum opening angle between the tool path and the horizontal plane(rad)		
d_1, d_2	distance between the highest point of the ridge and the lowest point of adjacent micro dimple(μm)		
$\boldsymbol{F}_{o_\mathrm{f}}^\mathrm{w}$	translational vector from $X_\mathrm{w}Y_\mathrm{w}Z_\mathrm{w}$ to $X_\mathrm{f}Y_\mathrm{f}Z_\mathrm{f}$		
$\boldsymbol{R}_\mathrm{w}^\mathrm{t}$	transformation matrix from $X_\mathrm{w}Y_\mathrm{w}Z_\mathrm{w}$ to $X_\mathrm{t}Y_\mathrm{t}Z_\mathrm{t}$		
$\boldsymbol{R}_\mathrm{f}^\mathrm{t}$	transformation matrix from $X_\mathrm{f}Y_\mathrm{f}Z_\mathrm{f}$ to $X_\mathrm{t}Y_\mathrm{t}Z_\mathrm{t}$		

1. Introduction

Titanium alloys including Ti-Al6-4V are now being widely used in different industries such as aviation, aerospace, optics and biomedical engineering due to their excellent mechanical properties. However, some studies demonstrate that the inherent characteristics of Ti-Al6-4V material such as the low thermal conductivity and high chemical reactivity result in accelerated tool wear and poor surface quality, e.g. see [1]. In order to address this problem, some non-traditional methods are applied to machine difficult to cut materials. Typical methods include electron beam machining, electrical discharge machining, laser machining, ultrasonic machining and others as explained in

[2-4]. Among them, ultrasonic machining is significantly efficient in machining with advanced, efficient, low machining cost and environmentally benign characteristics.

Ultrasonic Machining (UM) refers to a micron-level vibration assisted machining method where an additional excitation vibration (about 20 kHz) is generated from a tool or a workpiece, e.g. see [5-7]. It combines traditional machining such as turning [8,9], milling [10,11], grinding [12,13], drilling [14,15], polishing [16] with high-frequency ultrasonic vibration, which belongs to a composite machining method as studied in [13,17,18]. Besides, this technology has significant advantages in reducing cutting force, improving surface quality, prolonging tool life and eliminating burrs as described in [19,20]. At present, ultrasonic vibration assisted machining is widely used in the processing of difficult to cut materials, such as optical glass [21], nickel alloy [22], titanium alloy [23-25] and composite materials [12,26,27].

When compared with conventional machining, the most essential feature of UM is that it has a high-frequency relative vibration, which allows the tool and the workpiece to periodically separate during machining. This vibration transforms the traditional continuous cutting into high-frequency intermittent cutting. Moriwaki *et al.* [8] first applied one dimensional ultrasonic vibration cutting to turning operation. Nath *et al.* [28] proposed a contact rate model in ultrasonic assisted turning. In this model, the influence of machining and vibration parameters on the contact rate were studied. Experimental results showed that compared with conventional turning, tool life was increased by 4 to 8 times and surface finish quality was also significantly improved. Brehl *et al.* [29] investigated basic kinematic relationships of linear and elliptical ultrasonic vibration assisted cutting. The results indicated that a reduction of cutting forces and chip thickness was due to a periodic separation between the tool rake face and workpiece. In the ultrasonic vibration assisted turning, the separation mechanism between tool and workpiece is relatively simple. And this technique is widely used in one-dimensional and two-dimensional ultrasonic turning as described in [20].

However due to the continuous variation of cutting thickness and tool cutting velocity, an introduction of ultrasonic vibration makes the separation mechanism of milling complex. Feng *et al*. [30] analyzed the tool-workpiece separation and proposed three typical separation mechanisms. Through these analyses, Feng *et al*. [31,32] proposed novel models for the ultrasonic assisted milling to predict temperature and residual stress fields. Experimental results showed that high ultrasonic amplitudes and spindle speeds were the primary parameters that causing compressive residual stresses. In order to reveal the reason of cutting force reduction in the feed direction ultrasonic milling, Ni *et al.* [24] developed a kinematic model to describe tool and workpiece motions. The cutting time model was established through the kinematic analysis of the milling cutter and workpiece. The milling experiments showed that the ultrasonic force has a discrete pulse nature and when compared with CM, the amplitude of ultrasonic cutting force and surface roughness were lower.

Mathematical modelling and simulation serve as a theoretical support for experimental investigations as convincingly argued in [33-35]. The surface finish generated by CM is characterised by the tool marks due to the trochoidal trajectories of the tool tip whilst the ultrasonic surface finish is complex owing to the high-frequency vibration from the tool or the workpiece. Guo *et al.* [36] invented a tertiary motion generator for the elliptical vibration assisted turning. Subsequently, Guo *et al.* [17] investigated the influence of tool material on the elliptical vibration textures. It was noted that compared with the carbide inserts, better defined surface features can be achieved with the diamond insert due to a lesser elastic deformation and ploughing. Wang *et al.* [37,38] evaluated wear conditions of a grinding wheel using the fractal analysis approach. The experiments indicated that the fractal dimension of grinding wheel topography is highly related to the grain fracture, grain pullout, and wheel loading. Zhou *et al.* [39] developed a 3D ground surface topography generation method for the ultrasonic assisted grinding. Through those models, typical features of the ultrasonic ground surfaces analyzed. In the high-speed ultrasonic vibration cutting, Peng *et al.* [40] established a theorical model to analyze the intermittent cutting mode. Experimental results demonstrated that the high-speed ultrasonic vibration cutting has a better performance in reducing the cutting force, improving the tool life and surface finish quality when compared with CM. Zhang *et al.* [41] investigated the surface integrity using rotary ultrasonic elliptical end milling. It was found that the subsurface deformed layer and surface micro-hardness increased with the improved amplitude at low cutting speeds. According to the studies of Chen *et al.* [42], the ultrasonic surface textures were significantly affected by machining and ultrasonic vibration parameters. In addition, Shen *et al.* [43], Zhu *et al.* [44] also found that the micro textures can improve the surface tribological properties, especially the surface load capacity.

Recently, some researches have demonstrated that ultrasonic surface topographies are affected by tool-workpiece contact processes. Zhang *et al.* [45] generated the structured surfaces using two-stage vibration assisted turning. The experimental results indicated that the structure density defined by the aspect ratio of the micro dimples were approximated well by the simulation. Xu *et al.* [46] proposed a new rotary ultrasonic texturing technique and hybrid periodic micro/nano-textures were successfully fabricated on machined surfaces with one-point diamond tool. Kurniawan *et al.* [47] developed a two-frequency elliptical vibration texturing method, which improved the surface finish quality compared to conventional texturing method. Furthermore, Kurniawan et al. [48] and Lotfi *et al.* [49] investigated the structured patterns during the fabrication of microgrooves using a three-dimensional elliptical vibration (3D-EVT) method. Lu *et al.* [50] analyzed the effects of interference on the surface texture generation in the ultrasonic end milling. It was found that the feed interference greatly improved the surface texture so that the connectivity of the texture surface was enhanced. Yang *et al.* [19,51] developed abrasive workpiece contact rate model in tangential ultrasonic vibration assisted CBN grinding of ZrO_2 ceramics and proposed an ultrasonic surface topography model. In addition, a contrast experiment was undertaken to investigate the surface morphology of ultrasonic grinding and common grinding. In addition, Yan *et al.* [52] applied an external sinusoid excitation on the wheel to mitigate regenerative chatter in plunge grinding. In order to obtain a better surface quality, Ni *et al.* [1,23] applied minimum quantity lubrication(MQL) technique to ultrasonic milling. It was observed that the surface quality in UM&MQL was enhanced by about 20-30%. Feng *et al*. [53,54] investigated the conditions of surface roughness and tool wear. It was found that a lower spindle speed or a higher vibration amplitude will reduce the surface roughness. While the tool wear was accelerated at a high ultrasonic frequency and cutting speed.

Up to now, a comprehensive study on material remove process and surface generation mechanism of LTUAM is not available in the literature. Moreover, the effects of processing parameters, and particular, ultrasonic parameters on surface topography are ambiguous. In this investigation, the machining characteristics of material remove rate and the micro dimple generation process in LTUAM are analyzed through simulations and experiments. Specifically, tool angles including the clearance angle and the secondary cutting edge of the cutter are considered.

The remainder of the paper is organized as follows. In Section 2, the kinematics of material removal process of LTUAM is modelled and analyzed with respect to the tool tip trajectories. Then an analytical model for the tool-workpiece contact time is established. Furthermore, the micro dimpled surface generation process is investigated through numerical simulation in Section 3. Also, the effects of process parameters and tool angle on ultrasonic surface topographies are investigated. In Section 4 the experimental setup and procedure are introduced. In Section 5, some experimental investigations including cutting force, surface topographies and surface micro-hardness are presented, which is a good validation of the theoretical model. Some conclusions are drawn in Section 6.

2. Kinematic analysis of LTUAM

In order to understand material removal mechanism in the LTUAM, first the kinematic modelling and analysis are undertaken, specifically trajectories of the tool tip are modelled and analyzed. Then, the material removal process in each ultrasonic cycle of LTUAM is discussed through the tool workpiece contact rate model.

2.1 Analysis of the tool tip trajectories in LTUAM

The workpiece coordinate system $(X_\mathrm{w}Y_\mathrm{w}Z_\mathrm{w})$ is fixed on the workpiece as shown in Fig. 1(b). The feed coordinate system $(X_\mathrm{f}Y_\mathrm{f}Z_\mathrm{f})$ moves along the feed velocity with the workpiece coordinate system. The tool coordinate system ($X_t Y_t Z_t$) rotates around Z_f axis of the coordinate system $X_f Y_f Z_f$. In CM, the motion of the milling cutter with the workpiece consists of the feed motion and the tool rotation. The tool tip kinematic trajectories in CM can be expressed as:

$$\begin{cases} x_w(t) = x_0 + v_f t + R\sin(w_r t), \\ y_w(t) = y_0 + R\cos(w_r t), \\ z_w(t) = z_0, \end{cases} \tag{1}$$

where (x_0, y_0, z_0) is the initial position O_f of feed coordinate system with the point O_w of workpiece coordinate system, v_f is the feed velocity (mm/min), R is the tool radius (mm), w_r is the tool rotation angular velocity (rad/s), t denotes the motion time of the tool(s).

LTUAM adds longitudinal and torsional vibration to the directions of the tool axis and the cutting velocity, respectively, which is the main feature of two-dimensional ultrasonic vibration assisted machining. The tool tip kinematic trajectories of LTUAM in $X_t Y_t Z_t$ can be expressed as:

$$\begin{cases} x_t(t) = R\sin(w_r t + A\sin(w_f t + \varphi_1)/R), \\ y_t(t) = R\cos(w_r t + A\sin(w_f t + \varphi_1)/R), \\ z_t(t) = B\sin(w_f t + \varphi_2), \end{cases} \tag{2}$$

where A and B are the amplitudes of torsional and longitudinal ultrasonic vibration (μm), φ_1 and φ_2 are the initial phases of longitudinal and torsional vibration (rad), w_f represents the ultrasonic vibration angular velocity (rad/s).

According to Eqs (1) and (2), the tool tip kinematic trajectories of LTUAM in $X_w Y_w Z_w$ can be calculated by:

$$\begin{cases} x_w(t) = x_0 + v_f t + R\sin(w_r t + A\sin(w_f t + \varphi_1)/R), \\ y_w(t) = y_0 + R\cos(w_r t + A\sin(w_f t + \varphi_1)/R), \\ z_w(t) = z_0 + B\sin(w_f t + \varphi_2). \end{cases} \tag{3}$$

As shown in Figs 1(c) and (d), when A=0 and B=0, the longitudinal and torsional vibration disappear, and machining method becomes CM. When A=0, B=4μm, machining method belongs to LUAM, which is more common in drilling as discussed in [55]. While under the conditions of A=4μm, B=4μm, tool tip trajectories become more complex. In each ultrasonic cycle, the radial motion of the milling cutter can be regarded as a linear movement owing to the reason that the cutting velocity and ultrasonic vibration velocity are much higher than the feed velocity. In order to facilitate the analysis, the influence of the feed velocity is neglected here. A local coordinate system $O_1 X_1 Z_1$ is set to monitor the tool tip tracks along the axis of the milling cutter. O_1 is the equilibrium position at the initial moment of the cutting edge in ultrasonic vibration cycle. Z_1 axis is parallel to the tool axis, and X_1 axis is perpendicular to Z_t axis and tangent to the tool radius. Therefore, the tool tip kinematic trajectories in $O_1X_1Z_1$ can be expressed as:

$$\begin{cases} x_1(t) = v_c t + A\sin(w_f t + \varphi_1), \\ y_1(t) = B\sin(w_f t + \varphi_2). \end{cases} \tag{4}$$

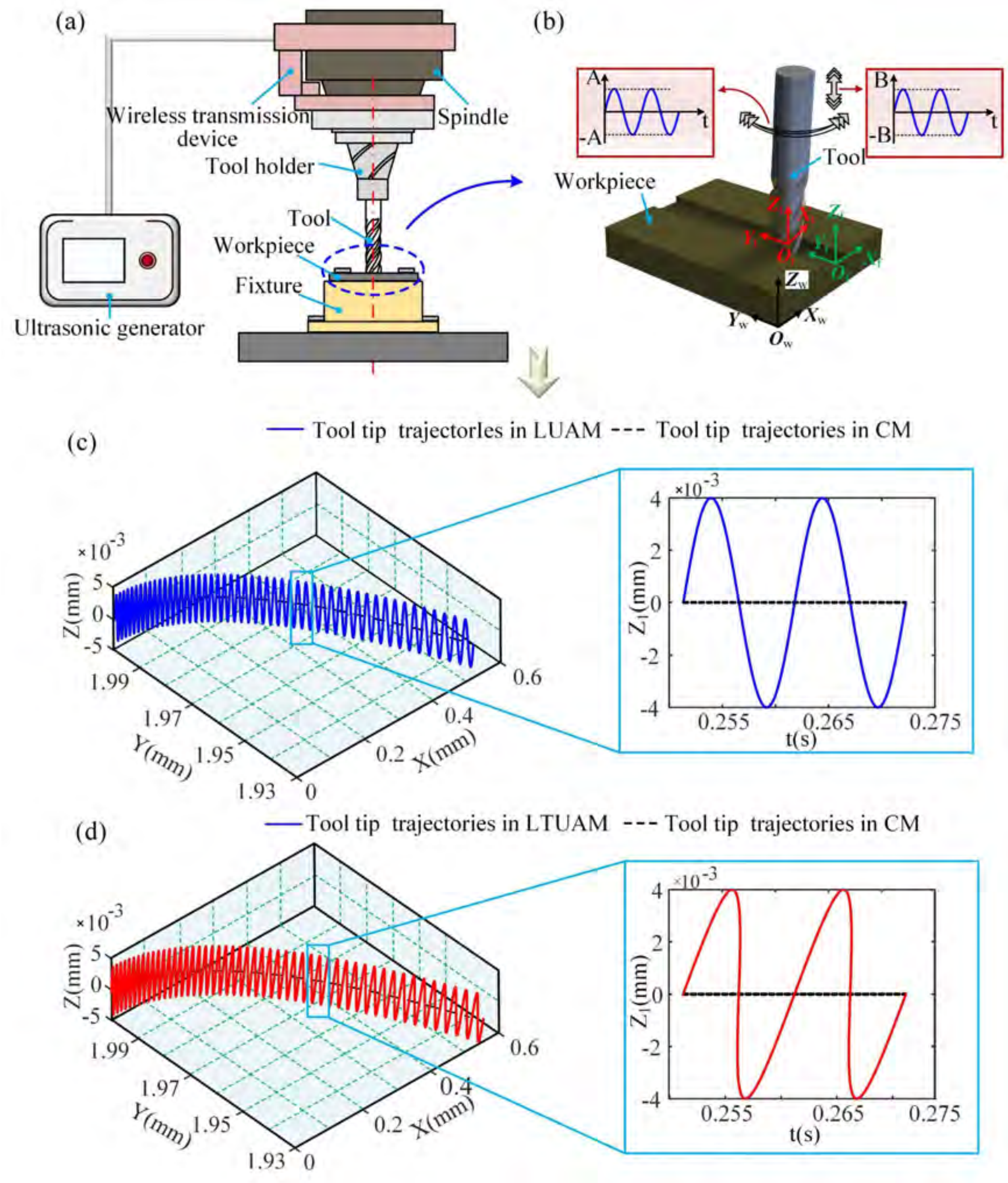

Figure 1. Modelling of the tool tip trajectories; (a) schematic of the LTUAM process; (b) establishment of the coordinate system; (c) and (d) are the tool tip trajectories in LUAM and LTUAM respectively for $f = 20\text{kHz}$, and $n = 2000\text{rpm}$.

In stable machining process, the rotary motion of the tool can be regarded as a uniform circular motion. And the cutting velocity v_c is constant and can be evaluated from a simple formula,

$$v_c = \frac{2\pi nR}{60}. \tag{5}$$

In $O_1X_1Z_1$, the trajectories of partially enlarged figure in LUAM and LTUAM are shown in Figs 1(c) and (d), respectively. From the perspective of kinematics, the tool tip trajectories in CM are straight lines. The tool tip trajectories in the longitudinal vibration milling are sine curves, while the tool tip trajectories in LTUAM are inclined sinusoids. As shown in Fig. 2, GH and G_sH_s are the tool cutting edge boundaries in LTUAM. The velocities v_r and v_a induced by ultrasonic vibration can be calculated as:

$$\begin{cases} v_r = Aw_f\cos(w_f t + \varphi_1), \\ v_a = Bw_f\cos(w_f t + \varphi_2). \end{cases} \tag{6}$$

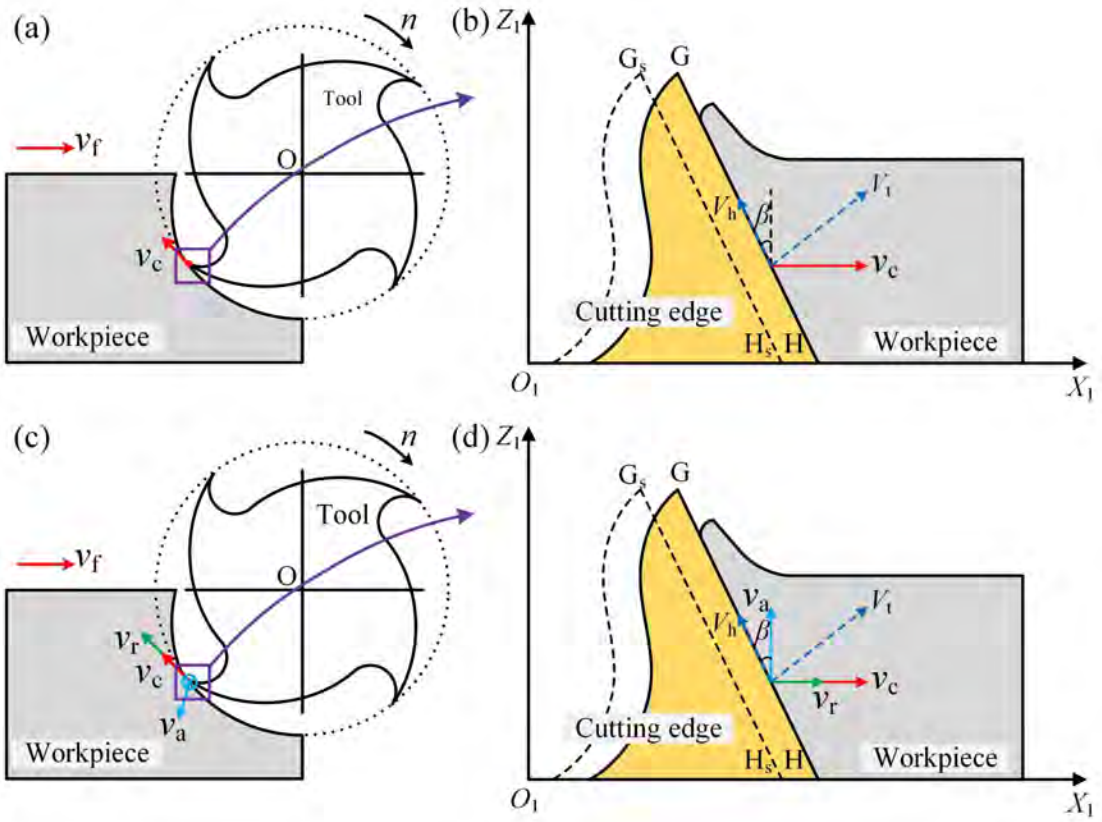

Figure 2. Kinematic analysis of LUTAM with schematic diagrams of the milling process for (a) CM and (c) LTUAM; velocity decomposition in the directions along the cutter and perpendicular to the cutter for (b) CM and (d) LTUAM.

As shown in Figs 2(a) and (b), in CM, the tool and workpiece kinematics include the feed motion and spindle rotation. The cutting speed is decomposed in the directions along the cutter and perpendicular to the cutter and can be expressed as:

$$\begin{cases} V_{\mathrm{t}} = v_{\mathrm{c}}\cos\beta, \\ V_{\mathrm{h}} = v_{\mathrm{c}}\sin\beta, \end{cases} \tag{7}$$

where V_{t} and V_{h} are the cutting velocity along the cutting edge and perpendicular to the cutting edge (m/s). In LTUAM, apart from the feed velocity and cutting speed, the motions of the tool with the workpiece are the torsional and longitudinal vibration velocities. As shown in Figs 2(c) and (d), the cutting speed and ultrasonic vibration velocities are decomposed and can be written as:

$$\begin{cases} V_{\mathrm{t}} = (v_{\mathrm{c}} + v_{\mathrm{r}})\cos\beta + v_{\mathrm{a}}\sin\beta, \\ V_{\mathrm{h}} = (v_{\mathrm{c}} + v_{\mathrm{r}})\sin\beta - v_{\mathrm{a}}\cos\beta, \end{cases} \tag{8}$$

where v_{r} and v_{a} are respectively the velocities caused by torsional and longitudinal ultrasonic vibration (m/s).

2.2 Analysis of the material removal process in LTUAM

In machining, chips are generated when the cutting edge of the milling cutter and the workpiece move in the direction along the tool helix angle as seen in [56]. In Eq. (7), v_{c} and β are constant values in CM. As shown in Fig. 3(a), it is assumed that the tool and workpiece are at position A in the initial moment where the tool and the workpiece are in contact. As time goes by, positive V_t means the tool is chasing the cutting face. Hence the cutting edge of the milling cutter reaches position B and chips are generated. In contrast, during LTUAM, the tool cutting edge will periodically change between GH and G_sH_s due to the effect of ultrasonic vibration, thereby the milling cutter and the workpiece will continuously contact and separate. Specifically, as pointed by Feng *et al*. [31], the conditions of contact or separation between the tool and the workpiece should be determined by the combination of velocity and displacement of the tool with the workpiece. Therefore, in order to determine whether the tool contact with the workpiece, as shown in Fig. 3(b), it is assumed that the tool and the workpiece just contact with each other at position A and $t_A = kT, (k = 0,1,2 \ldots)$, where T stands for ultrasonic vibration period. And B and C are the positions where V_{t} is zero. Based on the Fig. 3(c), the value of V_t of LTUAM is positive from position A to position B, which means that the tool is chasing the cutting face. In this time, the tool contacts with the workpiece. However, from position B to position C, the value of V_t in LTUAM is negative (see Fig 3. (c)). And the tool comes away from the workpiece. Hence the tool is separated with the workpiece. Finally, the tool returns to the equilibrium position D from the farthest position C and one ultrasonic cycle is completed. The tool moves backward and forward continuously with the workpiece considering the ultrasonic vibration, which explains the kinematics of LTUAM.

As shown in Fig. 3(d), in order to determine whether there is no cutting occurrence at a specific helix angle, first the intersection of the milling cutter trajectory with the X_1-

axis should be determined. The cutting edge moves from point A to point D in an ultrasonic cycle. Since points A and D are on the X_1-axis, Eq. (9) can be formulated as:

$$\begin{cases} B\sin(w_\mathrm{f}t_\mathrm{A}+\varphi_2)=0, \\ t_\mathrm{D}=t_\mathrm{A}+T, \end{cases} \tag{9}$$

where t_A and t_D are start and end moments at each ultrasonic cycle (s), T denotes as the ultrasonic vibration period (s).

When the cutting edge moves to point B at time t_B, the cutting edge of the tool and tool tip motion trajectories are tangent. At time t_B, the combined velocity of the tool in the direction perpendicular to the cutting edge is zero, which can be given by:

$$(v_\mathrm{c}+Aw_\mathrm{f}\cos(w_\mathrm{f}t_\mathrm{B}+\varphi_1))\cos\beta+Bw_\mathrm{f}\cos(w_\mathrm{f}t_\mathrm{B}+\varphi_2)\sin\beta=0. \tag{10}$$

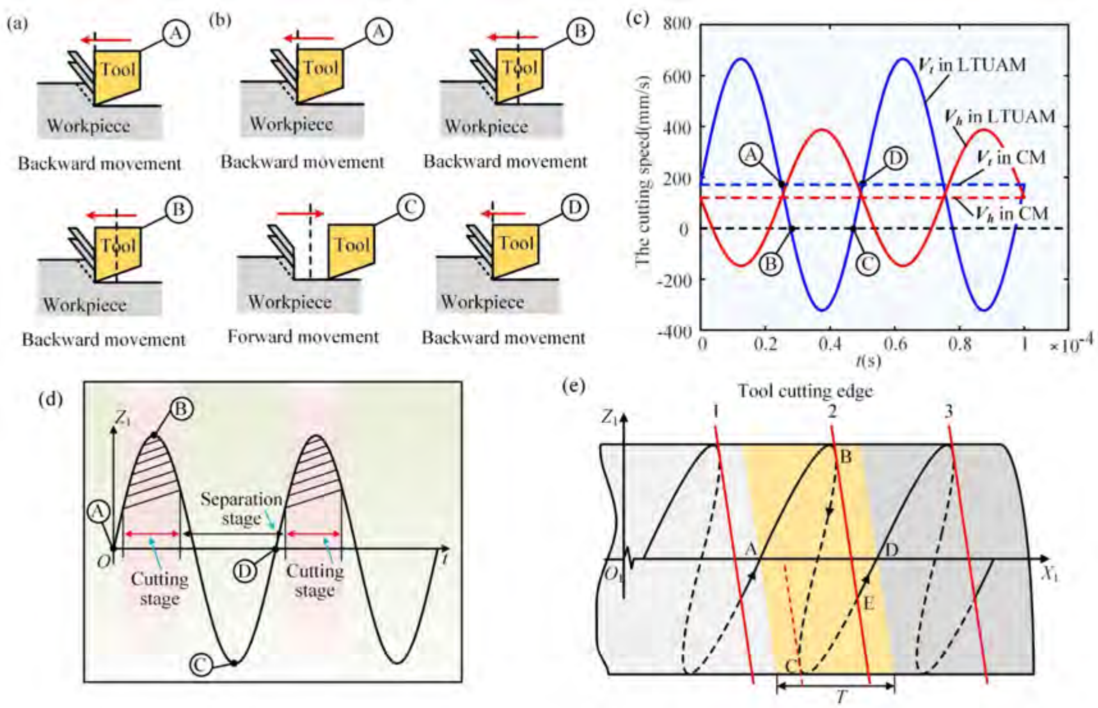

Figure 3. Kinematics of LTUAM process; (a) relative motion of CM between tool and workpiece; (b) relative motion of LTUAM between tool and workpiece; (c) critical cutting velocity with $f=20\mathrm{kHz}, n=1000\mathrm{rpm}$; (d) intermittent cutting process in adjacent vibration cycles in LTUAM; (e) material removal process in each vibration cycle.

Using Eqs (4) and (10), the coordinate of point B can be determined finally. Then the cutting edge moves from point B to point E, and its motion path is always on the left side of the line BE. Thence the cutting edge and the workpiece are always in a separate state. From Eq. (9), the coordinate of point D can be obtained as the intersection of the line BD and the tool tip motion trajectory. If the cutting edge reaches the point E at the time t_E. The equation descibing the line BD in $O_1X_1Z_1$ can be written as:

$$z = k_{\mathrm{BD}}(x - x_{\mathrm{B}}) + z_{\mathrm{B}}, \tag{11}$$

where $k_{\mathrm{BD}} = -\cot\beta$. According to the coordinate of point E obtained in Eq. (4), Eq. (11) can be expressed as:

$$\cot\beta(Rw_{\mathrm{r}}t_3 + A\sin(w_{\mathrm{f}}t_{\mathrm{E}} + \varphi_1) - x_{\mathrm{B}}) + z_{\mathrm{B}} - B\sin(w_{\mathrm{f}}t_{\mathrm{E}} + \varphi_2) = 0. \tag{12}$$

Then the separation time t_{s} can be expressed as a time difference when the cutting edge was at those respective locations:

$$t_{\mathrm{s}} = t_{\mathrm{E}} - t_{\mathrm{B}}. \tag{13}$$

Now, the tool workpiece contact rate r can be given by:

$$r = 1 - \frac{t_{\mathrm{s}}}{T} = 1 - \frac{t_{\mathrm{E}} - t_{\mathrm{B}}}{T}. \tag{14}$$

According to Eqs (4), (10) and (14), it can be concluded that the tool workpiece contact rate is affected by the ultrasonic frequency f, the ultrasonic amplitude A and B, the tool helix angle β, and spindle speed n. Fig. 4 shows the effects of different parameters on the tool workpiece contact rate. In Fig. 4(a), three different amplitudes of 2,4 and 6μm are set and as a result, the contact rate r is increased from 0.340 to 0.7659 at the spindle speed $n = 1200.53\mathrm{rpm}$. It can be observed that the spindle speed is correlated with the contact rate r. As the spindle speed is increased, the ultrasonic vibration effect is weakened and the cutting speed perpendicular to cutting edge direction increases. Thence the cutting time and contact rate increase. As illustrated in Fig. 4 (b), the tool helix angle affects the decomposition of the velocity vectors. It can be concluded that the cutting time for a large tool helix angle in the LTUAM is lower than that for a small tool helix angle.

Figs 4(c) and (d) plot the effects of ultrasonic parameters on the tool workpiece contact rate. It can be seen that as the ultrasonic amplitude and frequency are increased, tool workpiece contact rate r drops up quickly. The main reason is consistent with the variation of spindle speed. Besides, under the spindle speed $n = 2000\mathrm{rpm}$, the tool workpiece contact rate for 20.25kHz and 39.75 kHz are found to be about 0.4655 and 0.3064, respectively. The net cutting time is reduced about 51.9% in each ultrasonic cycle with the increased frequency from 20.25kHz to 39.75kHz. This means that the tool experiences a short duration of the pulsating cutting force when applying high ultrasonic frequency as explained in [24] and [28]. Fig. 4(d) shows the three-dimensional surface diagram of vibration amplitudes on the contact rate r in LTUAM process. It can be noted that when vibration amplitudes are small, the contact rate r maintains value 1. As vibration amplitudes are increased, the contact rate r becomes small. Therefore, vibration amplitudes have a great influence on the contact rate r.

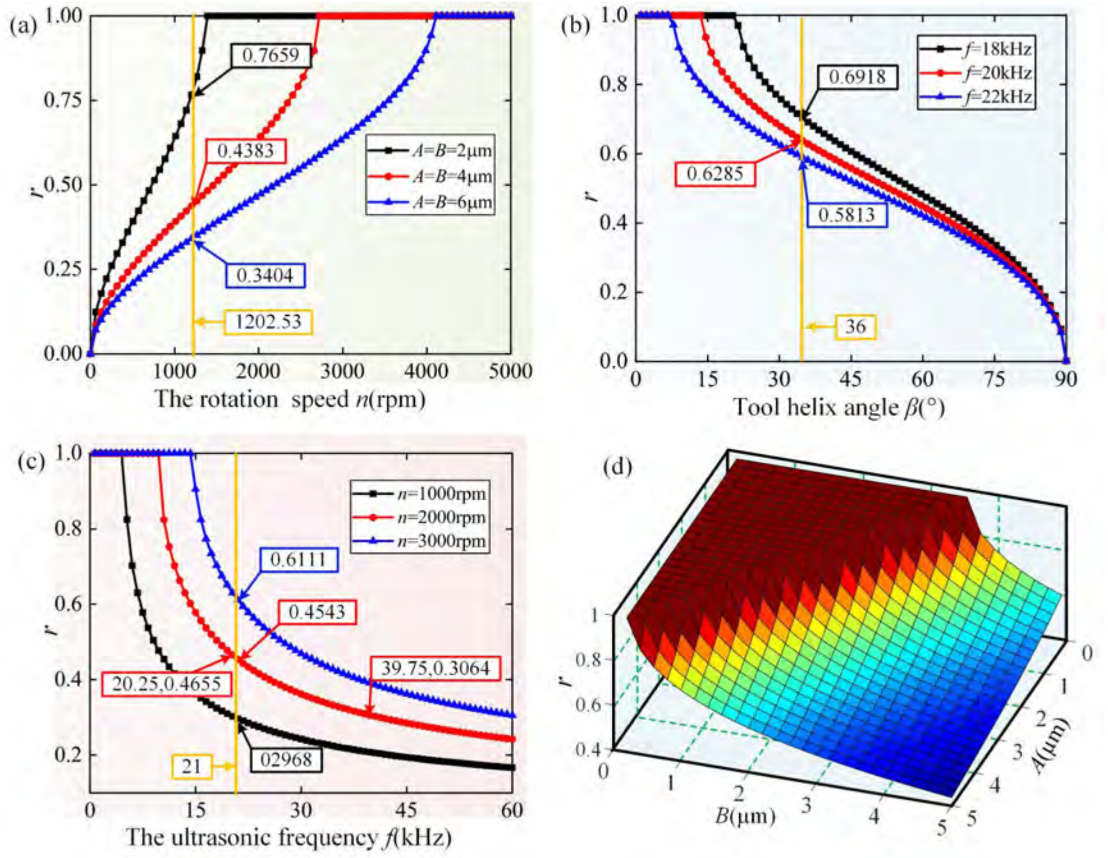

Figure 4. Effects of different parameters on the tool workpiece contact rate r;(a) spindle speed($f = 20\mathrm{kHz}, A = B = 6\mu\mathrm{m}$), (b) tool helix angle ($n = 2000\mathrm{rpm}, A = B = 4\mu\mathrm{m}$); (c) ultrasonic frequency ($n = 1000\mathrm{rpm}, A = B = 6\mu\mathrm{m}$); (d) ultrasonic amplitudes ($f = 20\mathrm{kHz}, n = 1500\mathrm{rpm}$).

3. Micro dimpled surface generation model

In this section, the relative motion between the tool and the workpiece and the mathematical description of the tool cutting edge are studied systematically. Finally, the ultrasonic surface topography prediction model is established considering the tool angles, which is also applicable in CM.

3.1. Coordinate transformation

The tool moves from $X_\mathrm{w}Y_\mathrm{w}Z_\mathrm{w}$ to $X_\mathrm{f}Y_\mathrm{f}Z_\mathrm{f}$ at a fixed feed velocity. Thence the translational vector can be calculated as:

$$\boldsymbol{F}_{o_\mathrm{f}}^{\mathrm{w}} = \begin{bmatrix} v_\mathrm{f}t \\ 0 \\ 0 \end{bmatrix}. \tag{15}$$

The tool coordinate system ($X_\mathrm{t}Y_\mathrm{t}Z_\mathrm{t}$) rotates with Z_f axis of the coordinate system $X_\mathrm{f}Y_\mathrm{f}Z_\mathrm{f}$. Therefore the rotational transformation matrix from $X_\mathrm{f}Y_\mathrm{f}Z_\mathrm{f}$ to $X_\mathrm{t}Y_\mathrm{t}Z_\mathrm{t}$ can be expressed as:

$$\boldsymbol{R}_{\mathrm{f}}^{\mathrm{t}}=\begin{bmatrix}\sin\theta & -\cos\theta & 0\\ \cos\theta & \sin\theta & 0\\ 0 & 0 & 1\end{bmatrix}. \tag{16}$$

According to Eqs (15) and (16), the transformation matrix from $X_{\mathrm{w}}Y_{\mathrm{w}}Z_{\mathrm{w}}$ to $X_{\mathrm{t}}Y_{\mathrm{t}}Z_{\mathrm{t}}$ can be written as:

$$\boldsymbol{R}_{\mathrm{w}}^{\mathrm{t}}=\begin{bmatrix}\boldsymbol{R}_{\mathrm{f}}^{\mathrm{t}} & \boldsymbol{F}_{\mathrm{o}}^{\mathrm{w}}\\ 0 & 1\end{bmatrix}. \tag{17}$$

In the tool coordinate system, the discrete coordinate points of the tool cutting edge can be described as follows:

$$\boldsymbol{P}^{\mathrm{t}}=\begin{bmatrix}x_{\mathrm{m,n}}\\ y_{\mathrm{m,n}}\\ z_{\mathrm{m,n}}\end{bmatrix}, \tag{18}$$

where all details with regards to the coordinate points $[x_{\mathrm{m,n}}, y_{\mathrm{m,n}}, z_{\mathrm{m,n}}]$ will be explained in Section 3.2. Therefore, the discrete points of the tool cutting edge in $X_{\mathrm{w}}Y_{\mathrm{w}}Z_{\mathrm{w}}$ can be given as:

$$\boldsymbol{P}^{\mathrm{w}}=\boldsymbol{R}_{\mathrm{w}}^{\mathrm{t}}\begin{bmatrix}\boldsymbol{P}^{\mathrm{t}}\\ 1\end{bmatrix}. \tag{19}$$

After the motion between the tool and the workpiece is established, the tool and the workpiece should be discretized. Some detailed discussions can be found in Section 3.2.

3.2. Description of tool geometry

The tool clearance angle is a key factor in the process of forming surface texture. Some studies simplified the tool cutting edge as a straight line and arc as explained in [43]. However, this is insufficient for LTUAM due to the phenomenon of recutting effect e.g. see [35]. Considering the longitudinal vibration of the tool, the 3D topography of the tool should be discretized. In the process, the secondary cutting edge and the clearance angle of the tool are the primary contact parts between the tool and the workpiece, therefore they are considered in the simulated model. Besides, the heights of the discrete points are different due to the structure of the milling cutter. In the tool radial direction, the cutting edge is also discretized into discrete points. It can be seen from Fig. 5(a) that the secondary cutting edge of the tool is simplified into a straight line and a circular arc. In each circumferential direction, the tool is expanded in the circumferential direction in Fig. 5(b). The clearance angle makes the discrete points of the tool have different height values. The arc length $l_{\mathrm{m,n}}$ that the tool is expanded in the circumferential direction can be expressed as:

$$l_{\mathrm{m,n}}=\theta_{\mathrm{m,n}}r_{\mathrm{m,n}}, \tag{20}$$

where $\theta_{\mathrm{m,n}}$ and $r_{\mathrm{m,n}}$ are the radian and radius at position (*m*,*n*). *m* and *n* are the number of discrete points in the tool radial direction and the circumferential direction, respectively. m=1, 2 ,…, M_1; n=1, 2,…,N_1.

As shown in Fig. 5(c), the cutting edge of the tool is discretized as grid points as follows:

$$\begin{cases} x_{\mathrm{m,n}} = r_{\mathrm{m,n}}\cos\theta_{\mathrm{m,n}}, \\ y_{\mathrm{m,n}} = r_{\mathrm{m,n}}\sin\theta_{\mathrm{m,n}}. \end{cases} \tag{21}$$

Considering the influence of ultrasonic vibration and the tool clearance angle on the height value in $X_{\mathrm{t}}Y_{\mathrm{t}}Z_{\mathrm{t}}$, the value of secondary cutting edge $z_{\mathrm{m,n}}$ can be written as:

$$\begin{cases} l_{\mathrm{m,n}}\tan\alpha - r_{\mathrm{m,n}}\tan\kappa + x_1\tan\kappa + r_{\mathrm{e}}(1-\cos k), 0 < r_{\mathrm{m,n}} \le x_1, \\ l_{\mathrm{m,n}}\tan\alpha + r_{\mathrm{e}},\ x_1 < r_{\mathrm{m,n}} \le R, \end{cases} \tag{22}$$

where $x_1 = R - r_{\mathrm{e}} - r_{\mathrm{e}}\sin\kappa$. α denotes as the clearance angle of the tool (rad), κ represents the angle of the secondary cutting edge of the tool (rad).

As shown in Fig. 5(d), the workpiece is discretized into grid points and the original height of the workpiece is stored in each grid point. In Fig. 5(e), for the points in the cutting area, if the height of the cutting edge is lower than the height of the workpiece, the workpiece height value will be updated. Otherwise, the workpiece height value will be kept unchanged. The specific update strategy can refer to the studies of Buj-Corral *et al*. [57]. Therefore, the ultrasonic surface topography can be obtained through Eq. (23) as shown below,

$$\begin{bmatrix} x_{\mathrm{m,n}} \\ y_{\mathrm{m,n}} \\ z_{\mathrm{m,n}} \\ 1 \end{bmatrix}_{\mathrm{w}} = \boldsymbol{R}_{\mathrm{w}}^{\mathrm{t}} \begin{bmatrix} x_{\mathrm{m,n}} \\ y_{\mathrm{m,n}} \\ z_{\mathrm{m,n}} \\ 1 \end{bmatrix}_{\mathrm{t}} = \begin{bmatrix} v_{\mathrm{f}}t + r_{\mathrm{m,n}}\sin\left(w_{\mathrm{r}}t + A\sin(w_{\mathrm{f}}t+\varphi_1)/R + l_{\mathrm{m,n}}/R\right) \\ r_{\mathrm{m,n}}\cos\left(w_{\mathrm{r}}t + A\sin(w_{\mathrm{f}}t+\varphi_1)/R + l_{\mathrm{m,n}}/R\right) \\ z_{\mathrm{m,n}} + B\sin(w_{\mathrm{f}}t+\varphi_2) \\ 1 \end{bmatrix}, \tag{23}$$

where $\boldsymbol{R}_{\mathrm{w}}^{\mathrm{t}}$ denotes as the transformation matrix from $X_{\mathrm{w}}Y_{\mathrm{w}}Z_{\mathrm{w}}$ to $X_{\mathrm{t}}Y_{\mathrm{t}}Z_{\mathrm{t}}$ and $(r_{\mathrm{m,n}}, z_{\mathrm{m,n}})$ can be obtained from Eqs (21) and (22).

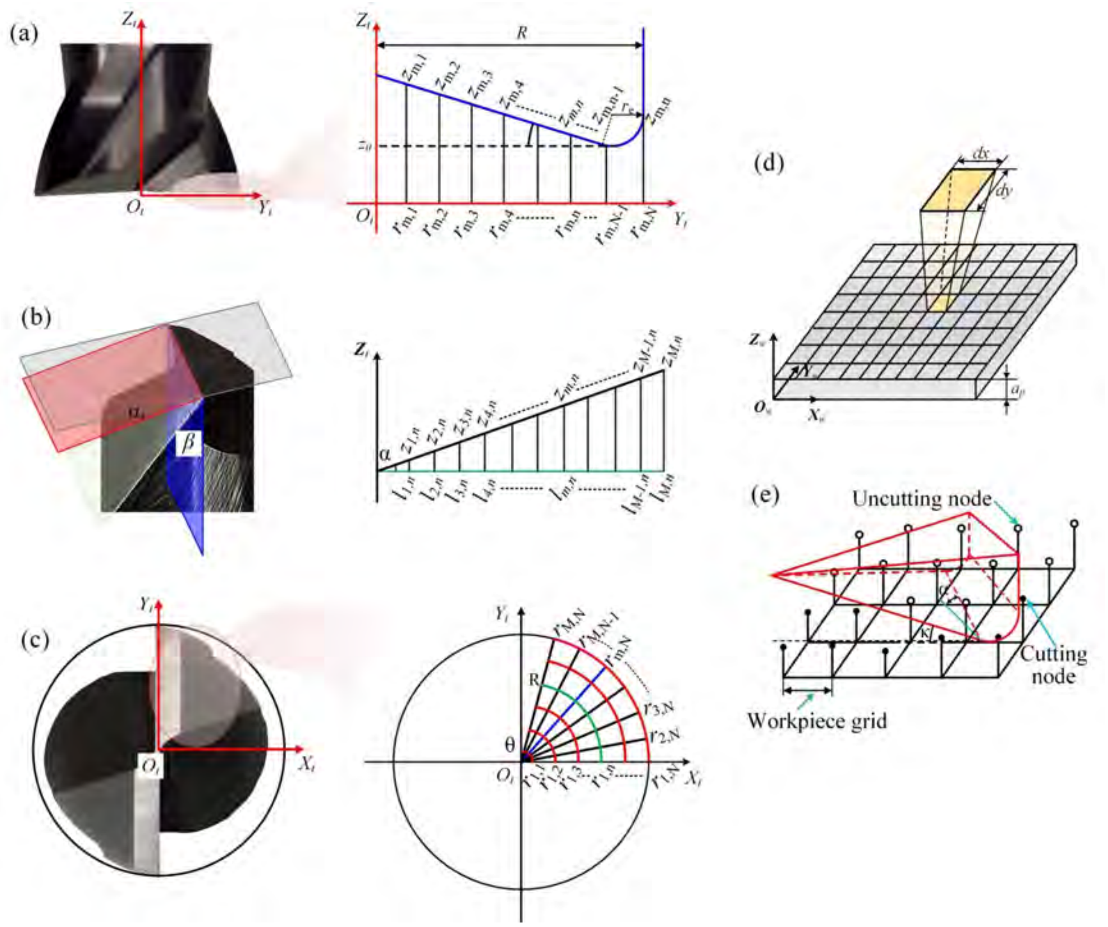

Figure 5. Discretization of the tool and the workpiece geometry; (a) clearance angle of the tool; (b) angle of the secondary cutting edge of the tool; (c) determination of the tool point cloud; (d) establishment of the workpiece point cloud; (e) update strategy of the workpiece point cloud.

3.3 Analysis of the micro dimpled surface generation process in LTUAM

The micro dimpled surfaces are affected by machining and vibration parameters. And it is essential to understand the textured surface generation process so that the textured surface can be designed quantitatively. In this section, generation process of micro dimpled structures is mainly analyzed from the geometric aspect including the size, shape and geometric position under different parameters. Guo *et al.* [17] firstly defined the parameter λ_1 during the elliptical vibration turning. This ratio, λ_1 is defined as the vibration frequency over the spindle rotation speed as

$$\lambda_1 = 60f/n = k_1 + \varepsilon_1. \tag{24}$$

where k_1 and ε_1 are the integer part and fractional part of λ_1.However, turning is different from milling owing to its different kinematics tool designs. In this paper, an improved definition of parameter λ_2 is given with respect to number of the tool teeth. The parameter λ_2 is the ratio of the ultrasonic frequency to the tool tooth frequency.

Besides, λ_2 can also be divided into an integer part k_2 and a fractional part ε_2, which can be expressed as:

$$\lambda_2 = 60f/nN = k_2 + \varepsilon_2, \tag{25}$$

where N is the number of the tool teeth.

As shown in Fig. 6(a), in the feed direction the distance of the micro dimples formed by two adjacent teeth is equal to the feed per tooth. In the cutting direction, the distance d between two adjacent dimples along the cutting velocity can be determined as:

$$d = \frac{v_{\mathrm{c}}}{f} = \frac{\pi Rn}{30f}. \tag{26}$$

According to Eq. (26), the larger distance d corresponds to higher spindle speed, which also results in a decrease in the density of the micro structures. Besides, the influences of ultrasonic frequency and the spindle speed on the value of d are opposite. In actual processing, the change of ultrasonic frequency is challenging due to the limitation of the resonance frequency of the ultrasonic structure. It is still essential to understand the effect of the ultrasonic frequency on the surface topography in LTUAM.

The phase shift distance of the adjacent dimples between the single tooth can be calculated from:

$$\delta_1 = \frac{\pi Rn\varepsilon_1}{30f}. \tag{27}$$

While the phase shift distance of the adjacent dimples between the adjacent tooth can be determined as:

$$\delta_2 = \frac{\pi Rn\varepsilon_2}{30f}. \tag{28}$$

As shown in Fig. 6(b), the maximum opening angle η between the tool path and the horizontal plane can be expressed as:

$$\eta = \mathrm{atan}\left(\frac{2A}{x_{\mathrm{F}} - x_{\mathrm{M}}}\right) = \mathrm{atan}\left(\frac{120Af}{\pi Rn - 120Af}\right). \tag{29}$$

where x_{F} and x_{M} are the abscissas of point F and M in $O_1X_1Z_1$. As shown in Figs 6(c)-(d), when $\alpha < \eta$, the tool clearance angle will intersect with the tool tip kinematic trajectories at point P. Nevertheless, when $\alpha > \eta$, there will be no intersection between the tool clearance angle and the tool tip kinematic trajectories.

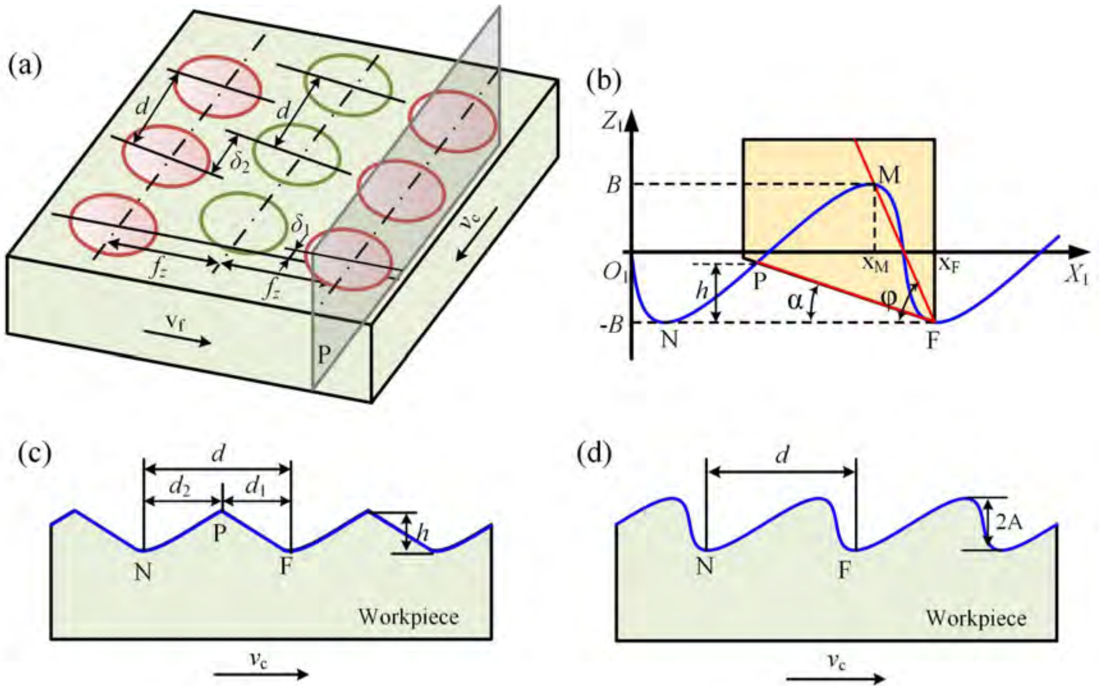

Figure 6. Quantitative analysis of the micro dimpled surfaces; (a) schematic of the micro dimples in LTUAM; (b) illustration of tool path; (c) and (d) cross-section profiles along the cutting direction for (c) $\alpha < \varphi$ and (d) $\alpha > \varphi$.

According to Fig. 6(c), when the recutting effect is found, the distance between two adjacent dimples consists of two parts, d_1 and d_2. Point F is the lowest point of the dimples. The coordinates of point F and point P can be obtained by Eqs (30), (31) and (32) as follows:

$$y_{\mathrm{P}} = (x_{\mathrm{P}} - x_{\mathrm{F}})\tan\alpha + y_{\mathrm{F}}, \tag{30}$$

$$x_{\mathrm{P}} = v_{\mathrm{c}} t_{\mathrm{P}} + A\sin(w_{\mathrm{f}} t_{\mathrm{P}} + \varphi_1), \tag{31}$$

$$z_{\mathrm{P}} = B\sin(w_{\mathrm{f}} t_{\mathrm{P}} + \varphi_2), \tag{32}$$

where value of t_{P} is determined by the position of point F. And when point F is determined, point P is also determined accordingly. So d_1 and d_2 can be expressed as:

$$\begin{cases} d_1 = x_{\mathrm{F}} - x_{\mathrm{P}}, \\ d_2 = d - d_1. \end{cases} \tag{33}$$

Finally, the value of h can also be calculated,

$$h = z_{\mathrm{P}} - z_{\mathrm{F}}. \tag{34}$$

3.4 Effects of process parameters and tool angle on ultrasonic surface topography

In this section, the effects of the process parameters and tool angle on the micro dimples are simulated. Specific parameters used in the simulation are shown in Table 1. The suitable size of mesh grid should consider the selection of machining and ultrasonic vibration parameters. In the simulation, ultrasonic amplitudes are the smallest physical value and they are set to 2 μm. In order to ensure the accuracy of the simulation, the size of the workpiece mesh grid is set to 0.5μm. In order to study the relationship of different parameters on the position and arrangement of the micro dimpled textures, some quantitative results are calculated based on the development presented in Section 3.3. As the result different values of the parameter λ_1 and λ_2 are obtained from simulations.

Table 1. Simulated parameters of surface textures for modelling LTUAM.

Parameters	
Spindle speed n(rpm)	1000,2000,3000,4000
Feed per tooth f_z(mm/Z)	0.01,0.02,0.03
Amplitude $A = B$(μm)	2
The tool clearance angle α(°)	0°,5°,10°
The angle of secondary the cutting edge κ(°)	0°,2.5°,5°
The blunt radius of the tool tip r_e(μm)	2

Fig. 7 shows ultrasonic surface topography simulations for LTUAM under low spindle speed of 1000 and 2000rpm. It can be observed that as the feed per tooth increases, the shape of the dimple becomes more wider in the feed direction. And the residual height of the machining workpiece surface increases, which is consistent with the variation in CM. In Figs 7(a)-(c), the arrangement of the micro dimpled texture is identical in the cutting direction. And micro dimples are overlapping and continuous in the feed direction. Furthermore, the values of both the parameter λ_1 and λ_2 are 0 in Figs 7(a)-(c), which is the main reason that the same arrangement of the micro structures is fabricated in the feed direction. In contrast, In Figs 7(d)-(f), the micro dimples are intermittent in the feed direction and staggered in the cutting direction. And the phase difference of the micro dimpled textures produced by the adjacent tool tooth is obviously found. At this time, the values of the parameter λ_1 and λ_2 are 0, 0.5, respectively. The values of simulated error are calculated according to Section 3.3 and listed in Table 2. In the simulation, the tool clearance angle is 10° and the length of the workpiece grid is 0.5μm. It can be found that the maximum error value of d is 1.6%. When compared with the previously reported models, the predicted surface topography generated by the method proposed in this paper is closer to the actual surface topography.

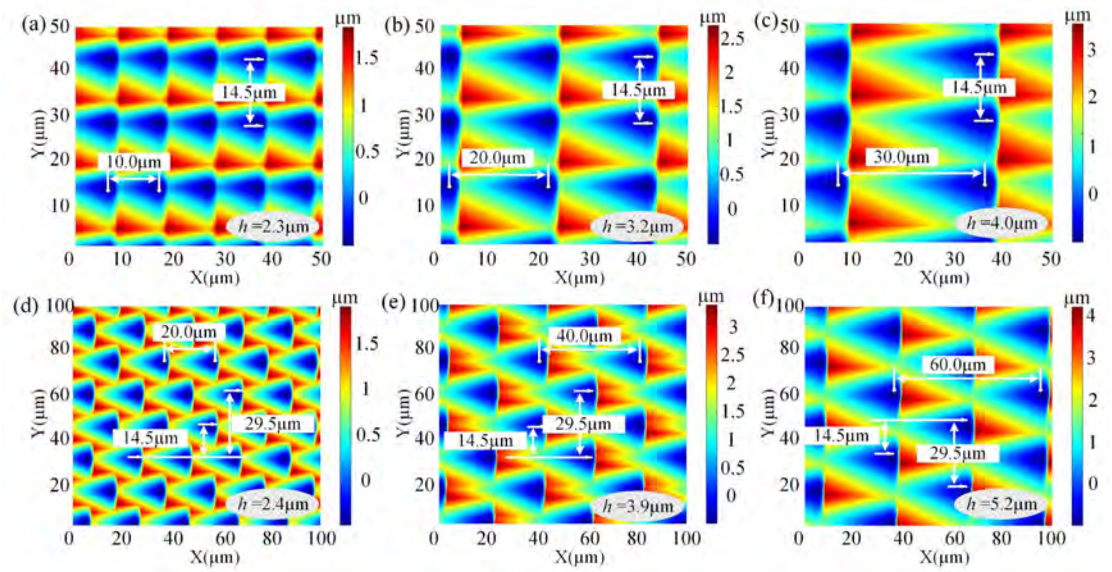

Figure 7. Micro dimpled texture simulations under the frequency $f = 21.3\text{kHz}$ and different spindle speed and feed per tooth in LTUAM. The feed per tooth of (a)-(c) are 0.01mm/Z, 0.02mm/Z, 0.03mm/Z, respectively, for the spindle speed $n = 1000\text{rpm}$; the feed per tooth in (d)-(f) varies from 0.01mm/Z, 0.02mm/Z, 0.03mm/Z, respectively, under the spindle speed $n = 2000\text{rpm}$.

Table 2 Values of the simulated errors for the surface topographies presented in Figure 7.

	(a)	(b)	(c)	(d)	(e)	(f)	(a)	(b)	(c)	(d)	(e)	(f)
	d(μm)						δ_1(μm)					
Theoretical value	14.74			29.49			0			0		
Simulated value	14.5			29.50			0			0		
The error	1.6%			0.03%			0			0		
	f_z(μm)						δ_2(μm)					
Theoretical value	10	20	30	10	20	30	0			14.75		
Simulated value	10.0	20.0	30.0	10.0	20.0	30.0	0			14.5		
The error	0	0	0	0	0	0	0			1.7%		

Fig. 8 depicts textured simulations for LTUAM under high spindle speeds of 3000 and 4000rpm. It can be found that dimensions of the micro dimples become large with the improved spindle speed in the cutting direction. Besides, when the spindle speed is increased, a longer distance can be observed in the cutting direction, which can be explained by the Eq. (26). According to Eqs (24) and (25), the values of k_1 and k_2 are decreased from 1278, 639 to 319, 159 with increase of the spindle speed, respectively. This will decrease the density of the micro dimpled textures. Furthermore, Figs 8(a)-(c) show the same discipline of the micro dimples with Figs 7(a)-(c). In Figs 8(d)-(f), the micro dimpled surface textures are arrayed with a greater deviation angle in feed direction. This phenomenon can also be explained by the values of λ_1 and λ_2. The values of λ_1 and λ_2 in Figs 8(d)-(f) are 0.5,0.75, respectively. According to Eqs (27) and (28), the phase shift distances in cutting direction are 29.49μm, 14.75μm, respectively. Hence in Fig. 8(d), when feed per tooth is small, the overlapping areas between the adjacent dimples are more obvious in the cutting and feed directions. However, when compared with the condition of $n = 3000$rpm, there is no significant increase in peak and valley values of h under $n = 4000$rpm. This is a beneficial effect to generate a better surface roughness. And the overlapping areas between adjacent dimples in the feed direction are reduced with the increase of feed per tooth.

The values of the simulated error for Fig. 8 are listed in Table 3 according to the modelling introduced in Section 3.3. The error values of δ_1, δ_2 and f_z in Figs 8(a)-(c) are both zero and the maximum error value of d is 5.6%. It can be noted that most of the errors are relatively small. Therefore, the simulation model is reliable and has a high accuracy. It can be concluded from Figs 7 and 8 that different surface structures can be obtained through the changing of machining and vibration parameters. And the values of λ_1 and λ_2 have a great impact on formation of the micro dimpled textures.

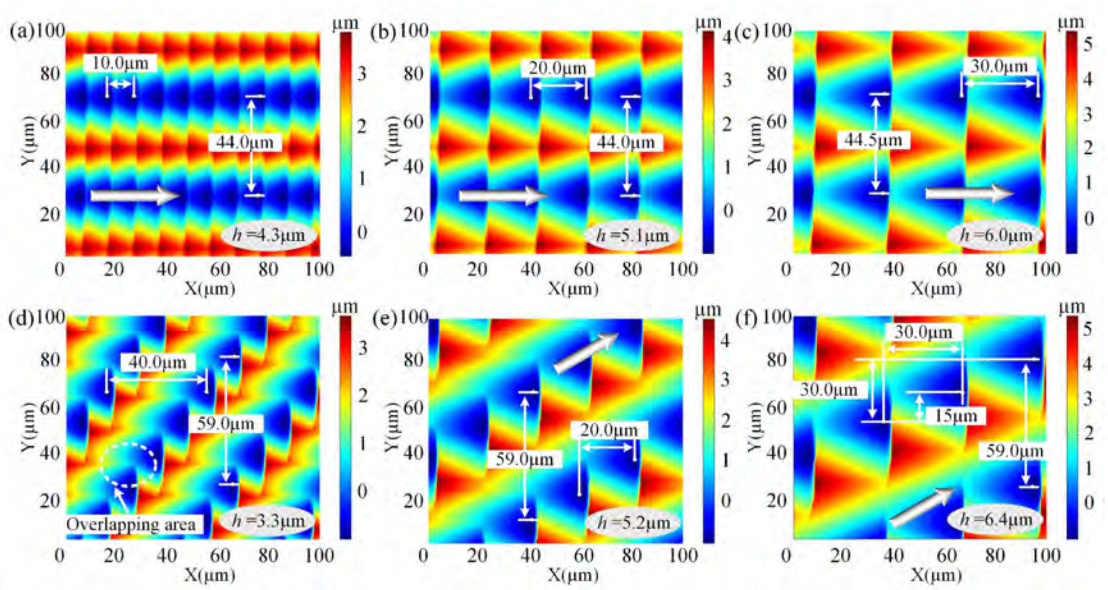

Figure 8. Micro dimpled texture simulation at the frequency $f = 21.3$kHz and different spindle speeds and feeds per tooth. The feed per tooth of (a)-(c) are 0.01mm/Z, 0.02mm/Z, 0.03mm/Z, respectively, under the spindle speed $n = 3000$rpm; The feed per tooth in (d)-(f) vary from 0.01mm/Z, 0.02mm/Z, 0.03mm/Z, respectively, with the spindle speed $n = 4000$rpm.

Table 3 Values of the simulated errors for the surface topographies presented in Figure 8.

	(a)	(b)	(c)	(d)	(e)	(f)	(a)	(b)	(c)	(d)	(e)	(f)
	d(μm)						δ_1(μm)					
Theoretical value	44.25			58.99			0			14.75		
Simulated value	44.0			59.0			0			15.0		
The error	5.6%			0.02%			0			1.69%		
	f_z(μm)						δ_2(μm)					
Theoretical value	10	20	30	10	20	30	0			29.49		
Simulated value	10.0	20.0	30.0	10.0	20.0	30.0	0			30.0		
The error	0	0	0	0	0	0	0			1.73%		

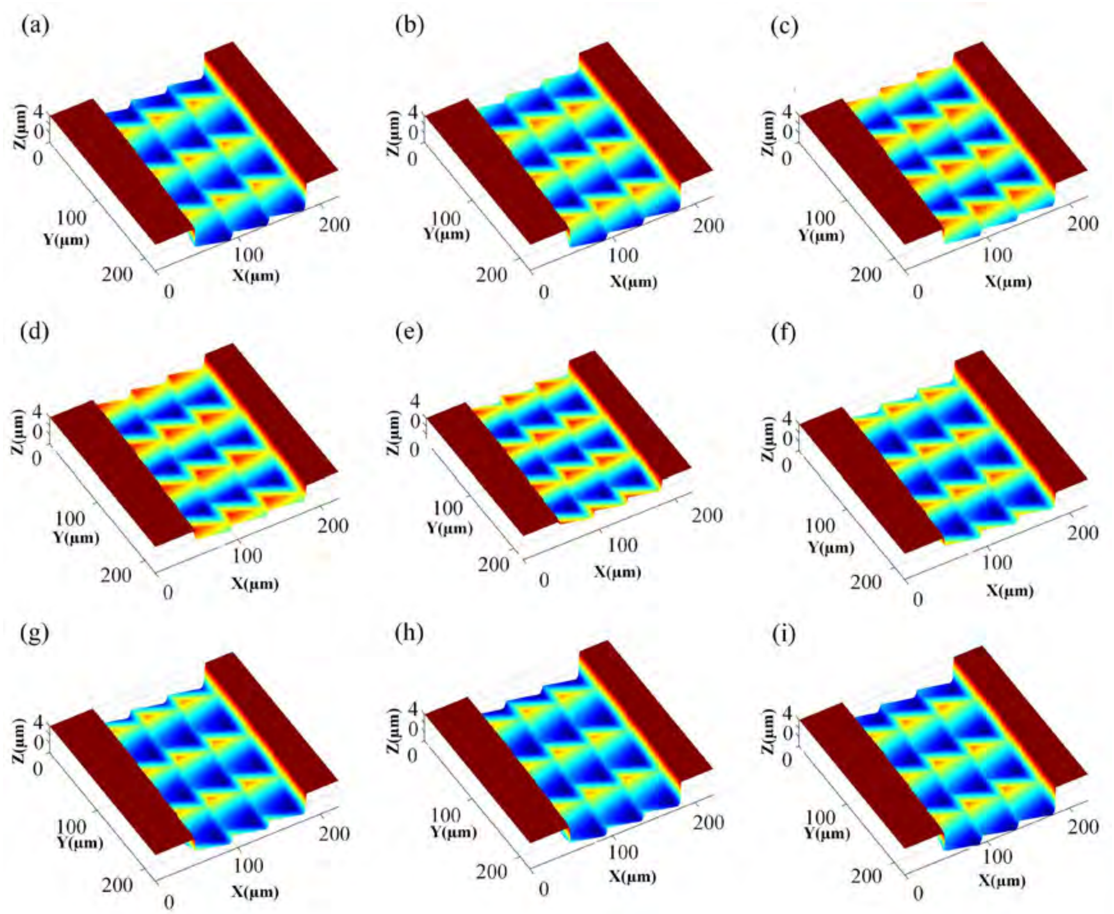

Figure 9. Micro dimpled topography generated by adjacent teeth at the frequency $f = 20\text{kHz}$ and spindle speed $n = 2000\text{rpm}$ and various phase differences of (a) 0, (b) 0.25π, (c) 0.5π, (d) 0.75π, (e) π, (f) 1.25π, (g) 1.5π, (h) 1.75π and (i) 2π.

The influence of the phase difference of the adjacent teeth on the ultrasonic surface topography is shown in Fig. 9, where the value of φ_1 is a constant, 0 and the value of φ_2 is varying between 0 and 2π. It can be seen that when the value of φ_2 changes between 0 and 2π, the micro dimples decrease firstly and then increase. And the smallest micro dimples can be obtained when the value of φ_2 is equal to 0.5π. In contrast, when the value of φ_2 varies between π and 2π, the micro dimples increase firstly and then decrease. And the biggest micro dimples can be obtained when the value of φ_2 is set to $3\pi/2$. In this paper, the longitudinal and torsional vibration are coupled together due to the structural design of the ultrasonic horn. The simulated analysis of the influence of the phase difference can be used to determine the phase difference accurately and guide the structural design of ultrasonic vibration equipment as studied in [58].

In addition, tool tip motion trajectories under different phase difference are analyzed in Fig. 10. It can be found that if the sum of phase difference satisfies $\varphi_1 + \varphi_2 = 2\pi$, the ultrasonic surface topography is the same due to periodic movement of the cutting edge.

However, the tool tip motion trajectories alone are not sufficient to reflect the formation of the ultrasonic surface topography. According to Fig. 9, the generation process of the machined surface is the combined results between the tool cutting edge and the workpiece. The 3D tool topography has a significant effect on the final machined topography. Therefore, a detailed discussion how the tool kinematics affects the surface topography is given below.

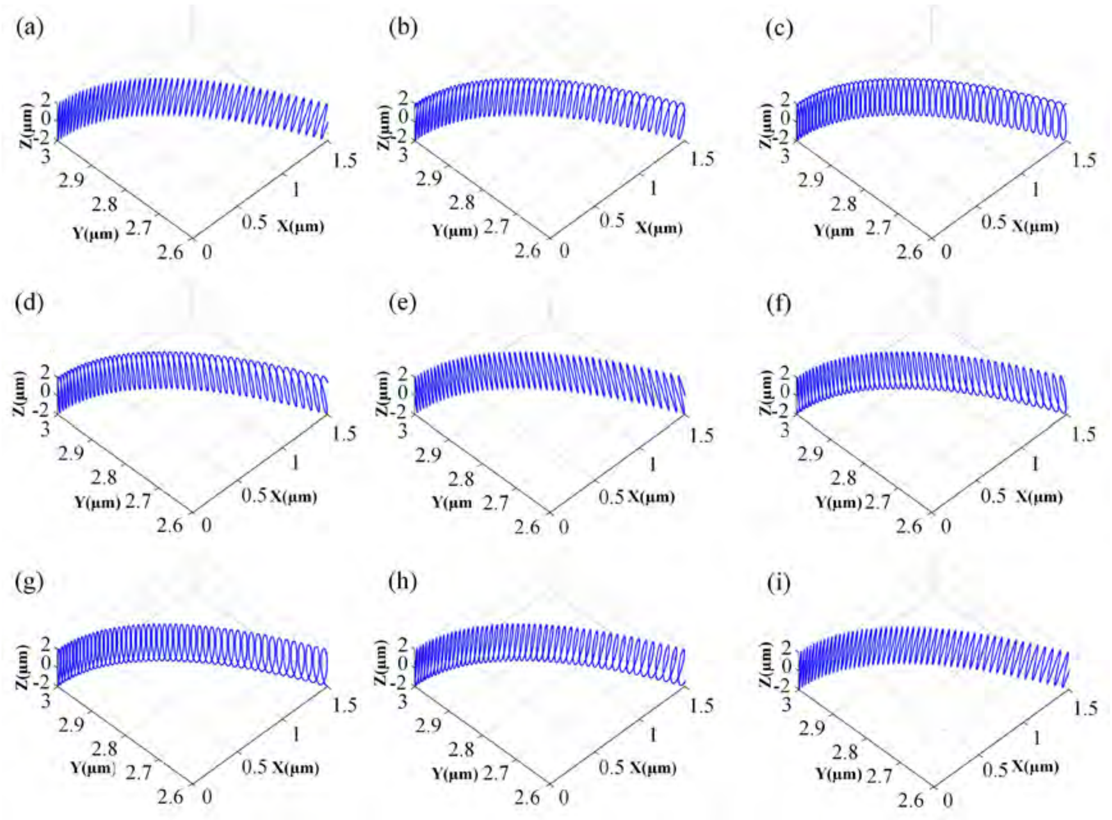

Figure 10. Tool tip trajectories at the frequency $f = 20$kHz, spindle speed $n = 2000$rpm and various phase differences of (a) 0, (b) 0.25π, (c) 0.5π, (d) 0.75π, (e) π, (f) 1.25π, (g) 1.5π, (h) 1.75π and (i) 2π.

To investigate the effect of the tool angles on the ultrasonic surface topography, different micro dimpled surfaces are obtained for different α and κ as shown in Fig. 11. It can be seen from Fig. 11(a) that when the value of κ is zero, the micro dimpled surfaces cannot be fabricated. This is because the workpiece materials are cut by the tool clearance angle in the cutting direction. However, as shown in Fig. 11(b), when the value of κ increased from zero to 2.5°, the micro dimples appear. Similarly, when the value of α is zero, recutting effect occurs and micro dimpled surfaces are not generated. As the value of α increases to 5°, micro dimples start to appear. Consequently it can be stated that bigger values of α and κ result in more obvious micro dimpled surfaces.

Fig. 11(e) depicts the surface topography under the same parameters as Fig. 11(d) without considering the tool clearance angle. It can be seen that the simulated surface topographies are different owing to the influence of the tool clearance angle. As shown in Fig. 11(f), the cross-section profiles obtained in Figs 11(d) and (e) are different from each other. And the value of η can be obtained to be 13.4° according to Eq. (29). Hence when the tool clearance angle is considered, the cutting edge of the tool interferes with the surface of the workpiece, which will further remove material. In general, the proposed simulation model is reliable and in order to obtain a good typography of micro dimpled surfaces, the values of α and κ must be set carefully.

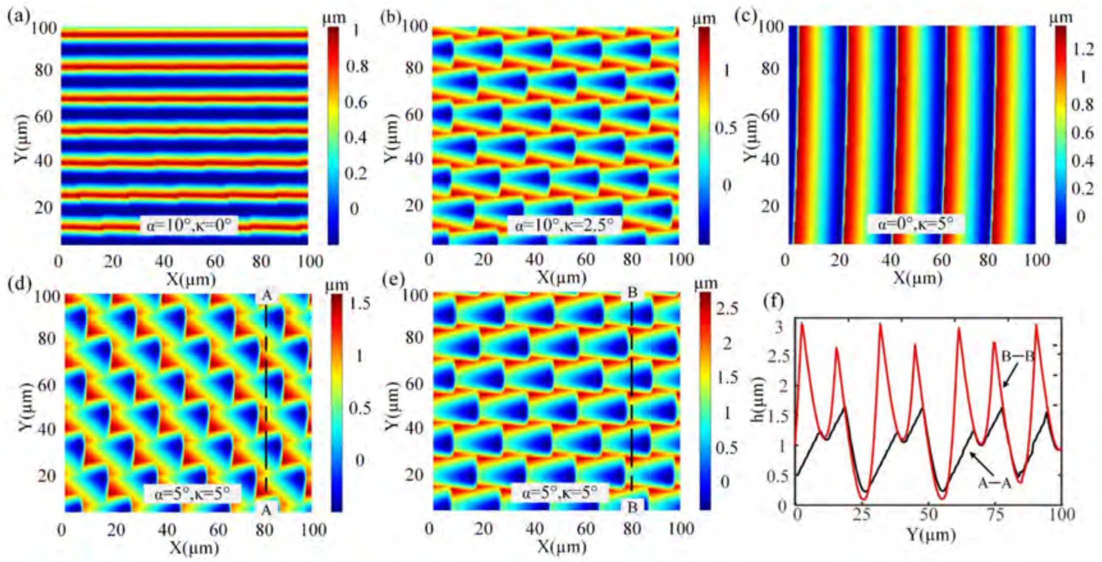

Figure 11. Influence of tool angle on the ultrasonic surface topography for frequency $f = 21.3\text{kHz}$ and spindle speed $n = 2000\text{rpm}$. The tool clearance angle α and secondary cutting edge angle κ are varied; (a) $\alpha = 10^{\circ}, \kappa = 0^{\circ}$, (b) $\alpha = 10^{\circ}, \kappa = 2.5^{\circ}$, (c) $\alpha = 0^{\circ}, \kappa = 5^{\circ}$, (d) $\alpha = 5^{\circ}, \kappa = 5^{\circ}$. (e) is obtained under the same parameters with (d) without considering the tool clearance angle. (f) depicts the cross-section profiles obtained in (d) and (e).

4. Experimental setup

Before the experimental studies were commenced, the ultrasonic vibration amplitude calibration was conducted as shown in Fig. 12(a). Vibration signals were collected by a laser displacement sensor with the sampling frequency is 80 kHz, where longitudinal and torsional responses were measured separately. The experimental results demonstrated that the ultrasonic head can provide a stable amplitude in the range between 0 and 5μm at frequency of 21.3 kHz, as shown in Figs 12(b) and (c). A high precision milling machine was used for all milling experiments of Ti-6Al-4V. The diameter of the carbide milling cutter used in the experiment was 6 mm with the helix angle of the cutter of 35°.

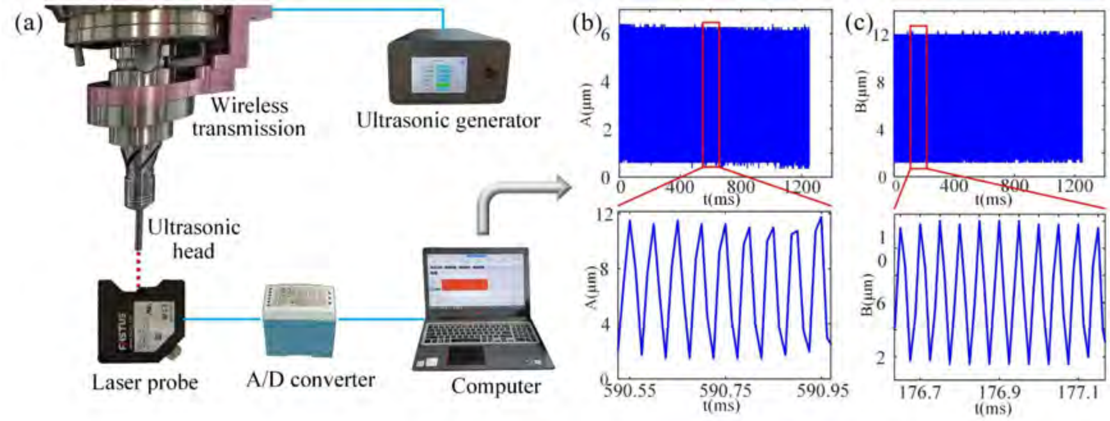

Figure 12. Amplitude calibration of the ultrasonic head; (a) vibration performance test setup; (b) and (c) are the measured ultrasonic amplitudes of longitudinal and torsional vibration, respectively.

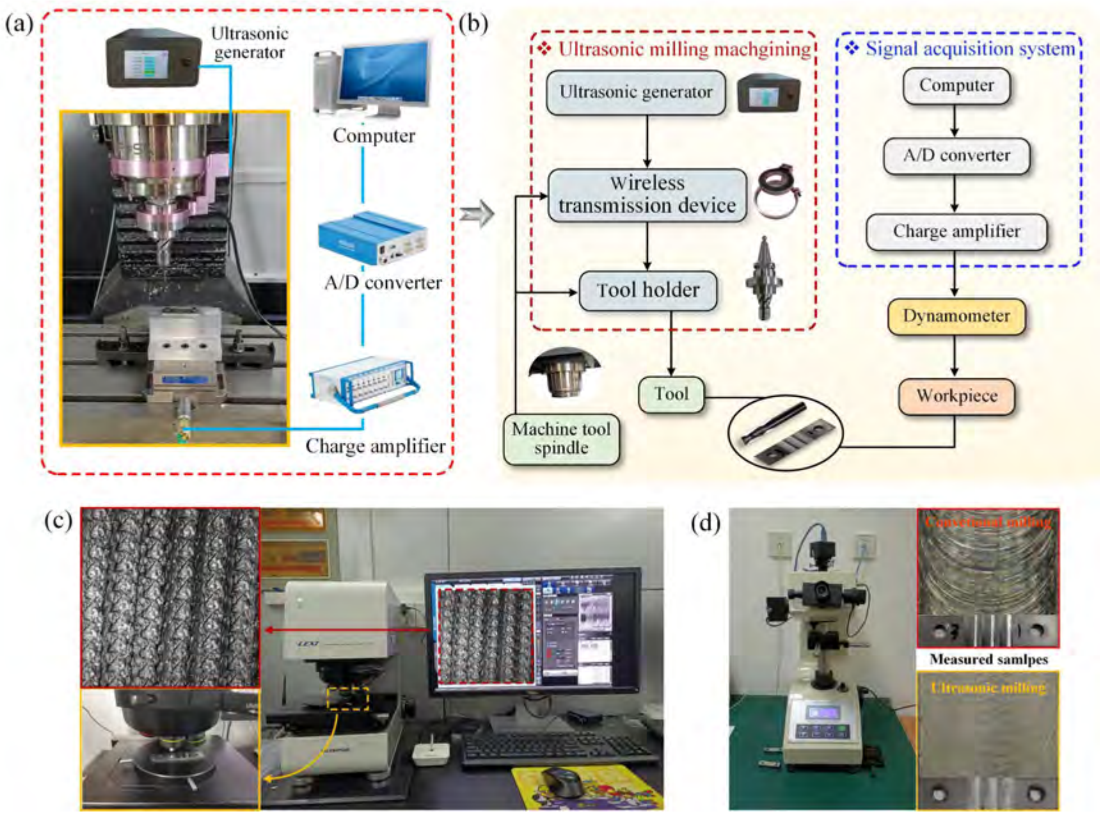

Figure 13. Experimental setup of LTUAM showing (a) experimental setup layout for LTUAM experiments, (b) block schematic of LTUAM experiments, (c) surface topography testing machine OLS4100, (d) hardness tester with measured samples.

The experimental setup of LTUAM is illustrated in Fig. 13(a) and it mainly consists of the ultrasonic milling machine and the signal acquisition system. As shown in Fig. 13(b), the LTUAM system includes an ultrasonic generator, a wireless transmission device and an ultrasonic vibration tool holder. The signal acquisition system is applied to collect the cutting force signal generated during the milling process. The sampling frequency of the dynamometer is set to 7 kHz and matching charge amplifier and data acquisition system are used to record the data. Experimental parameters and tool geometry for the end milling experiments are listed in Table 4. In the LTUAM process, the cutting force signals fluctuate within a certain range. The average cutting forces are utilized to analyze the effect of different machining parameters on the cutting force. After milling, the surface topographies are measured by a laser scanning confocal microscope shown in Fig. 13(c). And surface micro hardness values in both CM and LTUAM are measured by hardness tester, shown in Fig. 13(d), where the 500g load is applied to the indenter for 10s.

Table 4. Parameters and tool geometry for the end milling experiments.

Parameters	
Spindle speed n(rpm)	1000,2000,3000,4000
Feed per tooth f_z(mm/Z)	0.01,0.02,0.03
Amplitude A, B(μm)	1.5
Frequency f(kHz)	21.3
The tool clearance angle α(°)	10°
The angle of secondary the cutting edge κ(°)	5°
The blunt radius of the tool tip r_{e}(μm)	2

5. Discussion and results

In this section, the characteristics of material removal process and creating ultrasonically induced surface micro structures under different machining conditions will be analyzed. Modelling and experiments will be used to shed more lights on the nature of cutting forces, surface topographies and surface micro-hardness.

5.1 Comparison of milling forces in CM and LTUAM

The influences of different machining parameters in CM and LTUAM are investigated and shown in Fig. 14. Specifically, in Figs 14(a)-(c), both the milling force of CM and LTUAM are increased against the increased feed per tooth, and in LTUAM, the cutting force is significantly reduced. In order to eliminate the influence of the rotation position on the cutting force, the resultant force F_{t} and axial force F_{z} are used to analyze the experiment results. The resultant force F_{t} in the XOY plane can be expressed as:

$$F_{\mathrm{t}} = \sqrt{F_{\mathrm{x}}^2 + F_{\mathrm{y}}^2}. \tag{35}$$

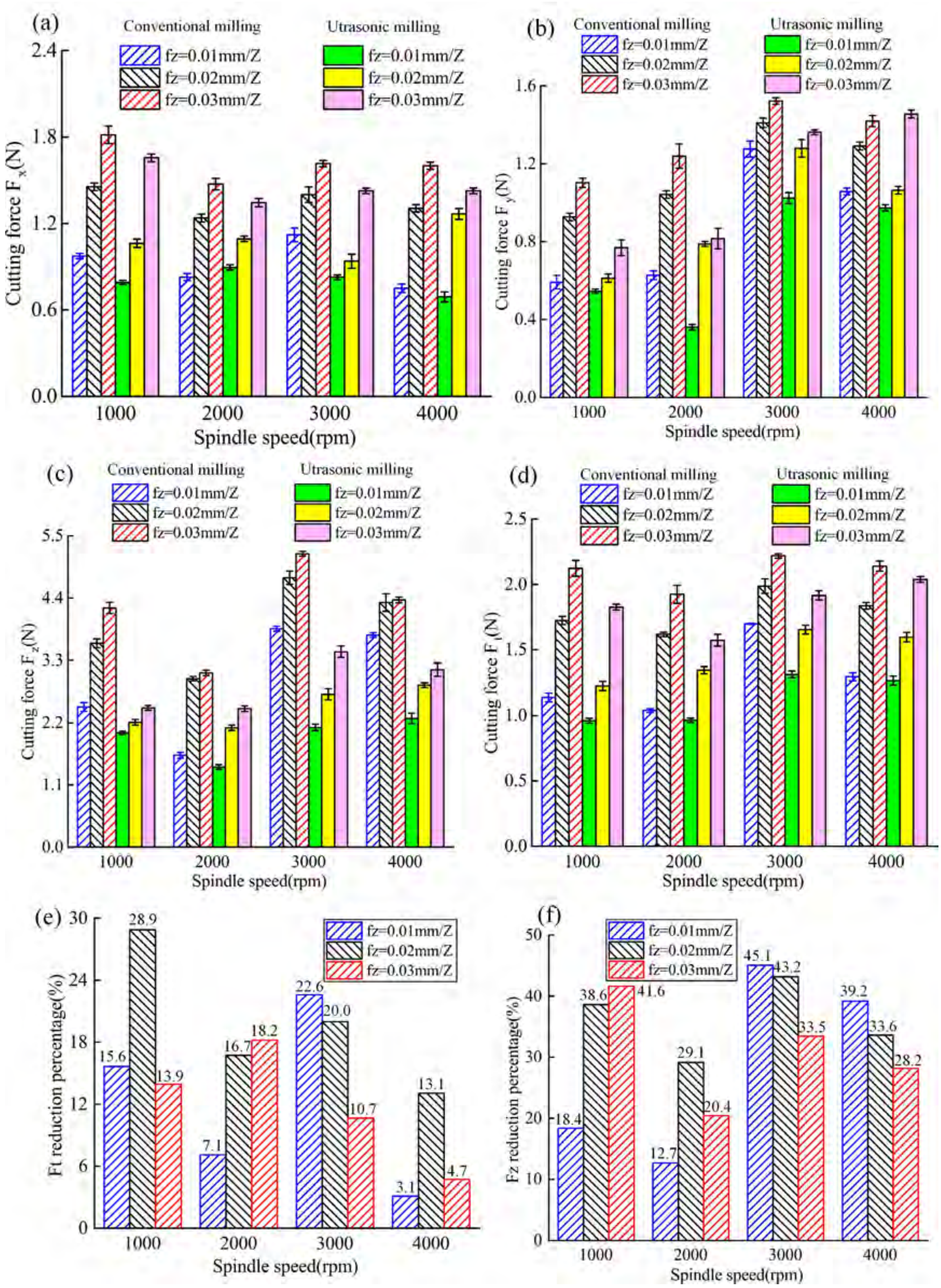

Figure 14. Comparison of cutting forces at different machining parameters; (a), (b) and (c) are the cutting force in x, y, z directions, respectively; (d) depicts the values of resultant force according to Eq. (33); (e) and (f) the reduction percentage of the resultant force F_t and axis force F_z.

Experimental data depicted in Figs 14(e) and (f) indicates that the tangential force and forces in LTUAM are reduced between 3.11% and 28.90% and 12.70% and 45.05%

respectively, when compared with CM. The reduction reason can be explained by the material removal mechanism in each ultrasonic cycle of LTUAM. As discussed in Section 2.2, the cutting forces are different in CM and LTUAM. The material removal of the tool cutting edge with ultrasonic vibration can change from continuous to discontinuous cutting as the tool and workpiece are separated in each ultrasonic vibration cycle. Besides, as is seen from Fig. 14(e), a more pronounced reduction of milling force can be observed at lower spindle speed. This can be attributed to the obvious separation effect, which facilitates a chip flowing and reduces a heat accumulation. As reported in [24], the amplitude of the cutting force can be also significantly reduced. In ultrasonic assisted milling processing, although the cutting thickness has a slight increase under the action of ultrasonic vibration as investigated in [59]. The formation of chips is significantly improved and the friction between the tool and the workpiece is reduced as shown in [60]. This has resulted in is a significant reduction of milling forces.

5.2 Verifying model of surface topography in LTUAM

Comparisons of the 2D surface morphologies at $n = 1000\text{rpm}$ and $n = 4000\text{rpm}$ in both CM and LTUAM are presented in Fig. 15. As shown in Figs 15(a)-(c), a large number of irregular feed trajectories and surface defects are clearly observed on the machined surface in CM due to the plowing and rubbing. By contrast, the machined surface appears substantial micro dimpled structures in LTUAM owing to the application of ultrasonic vibration. It is worth noting that due to the smaller angle of the secondary cutting edge and the material properties of the titanium alloy, there are plastic deformation of the machined material and metal plowing in Figs 15(j) and (k). And the formation of the micro dimpled structure is improved as the feed per tooth is increased at $n = 4000\text{rpm}$. In addition, the dimensions of the micro dimpled textures become more larger with the improvement of the spindle speed. And the residual height of the machined surface increases with the increased feed per tooth in both CM and LTUAM. As analyzed in Section 2.1 and 2.2, the processing mechanism in LTUAM is completely different to CM. The processing method, especially the tool tip trajectory, has a great influence on the surface characteristics. In addition, some functional features such as tribological performance and wettability were obtained by chosing relevant processing and vibration parameters from the literature [61,62].

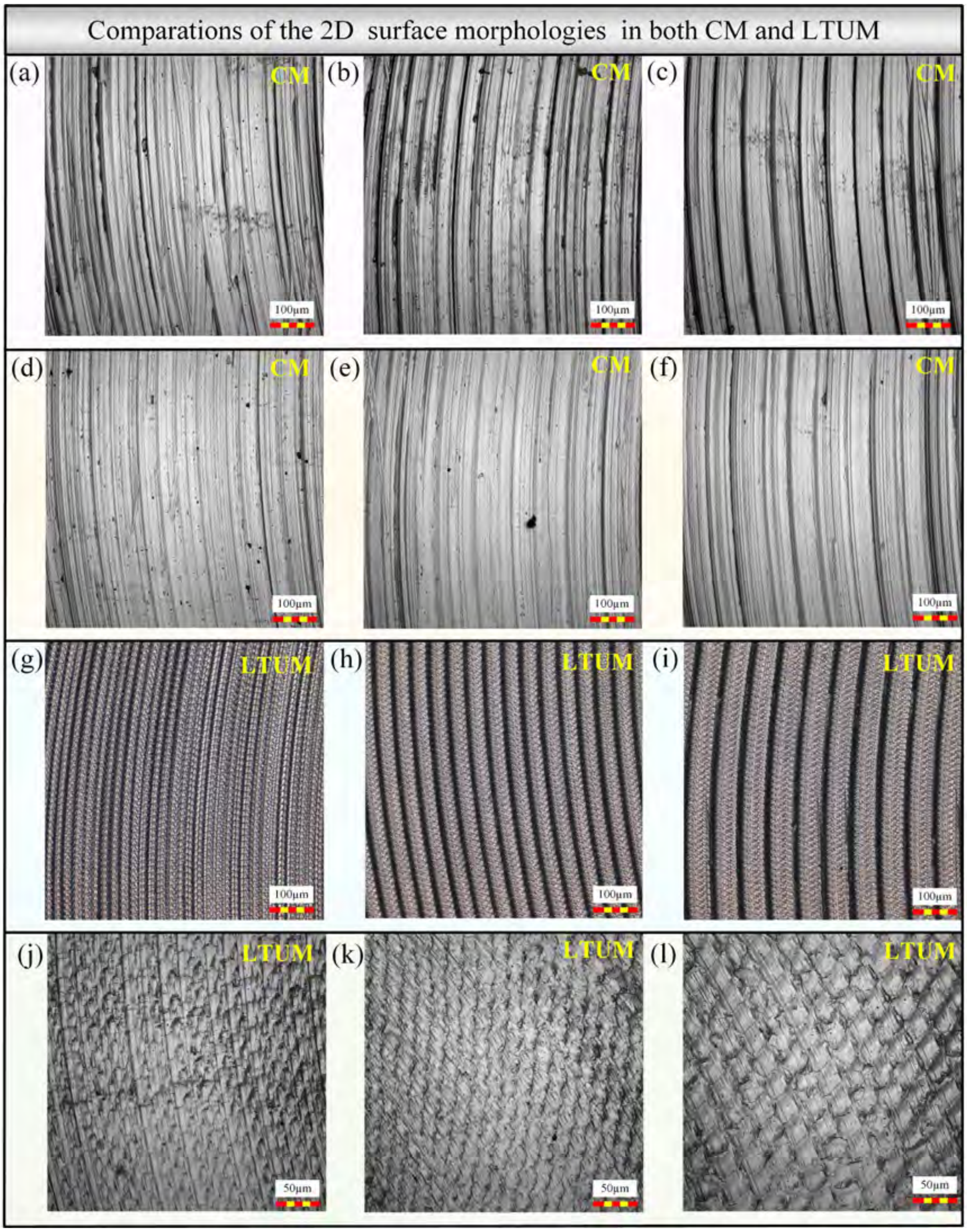

Figure 15. Comparisons of the 2D surface morphologies in both CM and LTUAM. Specifically, the feed per tooth of (a)-(c) and (g)-(i) are 0.01mm/Z, 0.02mm/Z, 0.03mm/Z, respectively, for the spindle speed$n = 1000$rpm; the feed per tooth in (d)-(f) and (j)-(l) are varying from 0.01mm/Z, 0.02mm/Z, 0.03mm/Z, respectively, with the spindle speed $n = 4000$rpm.

In order to the verify the model of surface simulation in Section 3, some typical morphologies of micro dimples are recorded under different parameters in Fig. 16. It can be observed that substantial micro dimpled textures are clearly found on the ultrasonic machined surfaces. The number of microstructures is reduced and dimension becomes larger with the increased spindle speed and this can be explained by reduction of k_1 and k_2. The values of the parameter λ_1 and λ_2 are 0 in Figs 16(a) and (c), thence the same micro dimples are fabricated in the feed direction and cutting direction. The arrangement of the phase difference of the micro dimples in Figs 16(b) and (d) produced by the adjacent tool tooth is obvious, which indicates the simulated micro dimpled surfaces are accurate. Furthermore, the surface profiles of experiment and simulation in LTUAM are also compared in Figs 16(c), (f), (i) and (l). It can be noted that simulation and experimental results are matched well. In Fig. 16, there are some irregular profiles which can be a side effect of the sampling strategies, which can influence 2D profiles. In the X direction, the same profiles for each feed are obtained from the simulation. However, in the Y direction, due to reason that sampling areas are small (256×256 μm^2) and the tool motion has trochoidal trajectories, irregular profiles may be obtained. Surface textures in LTUAM have micro dimples and ridges, which for perfectly matched process and ultrasonic parameters may result in unsmooth profiles. Besides, the 3D tool shape can cause that tool paths of LTUAM to interfere with the previous machining and this can also influence the 2D profiles. Experimental and simulation results of f_z and d are compared in Fig. 17. It can be found the deviation of f_z and d vary from 1.95% to 6.31% and from 2.03% to 4.29%, respectively. It is worth noting that tool wear and incomplete material removal are the primary reasons of theoretical and experimental deviation as explained in [11]. However, the simulated surface topographies shown in Figs 7 and 8 still demonstrate the primary characteristics of the micro dimples. This indicates that the simulation analysis is reliable.

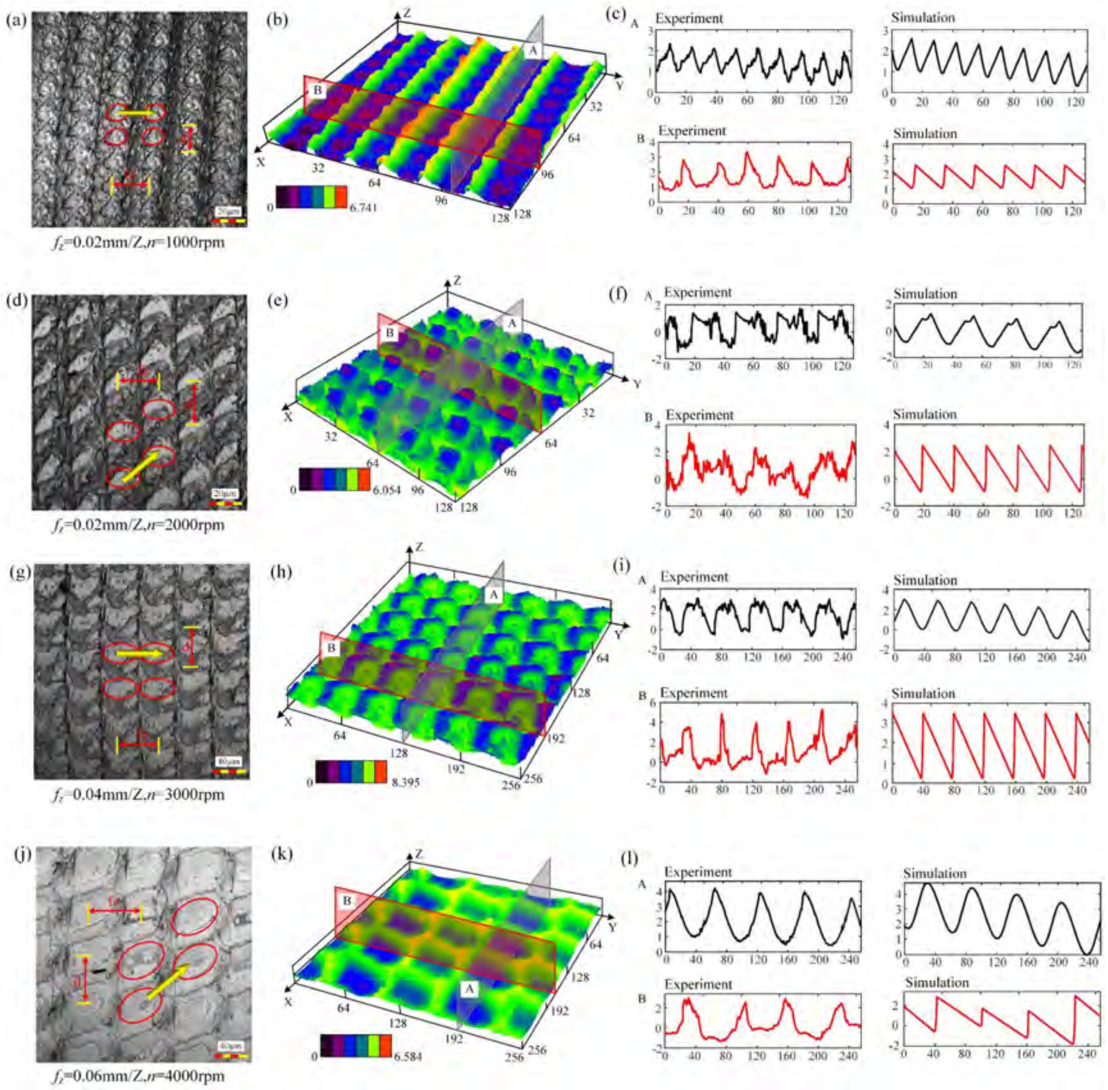

Figure 16. Some typical morphologies obtained under different spindle speed and feed per tooth, specifically, the parameters of 2D, 3D morphologies and surface profiles in LTUAM are respectively (a), (b) and (c): $f_z = 0.02\,\mathrm{mm/Z}, n = 1000\mathrm{rpm}$; (d), (e) and (f): $f_z = 0.02\,\mathrm{mm/Z}, n = 2000\mathrm{rpm}$; (g), (h) and (i): $f_z = 0.04\,\mathrm{mm/Z}, n = 3000\mathrm{rpm}$; (j), (k) and (l): $f_z = 0.06\,\mathrm{mm/Z}, n = 4000\mathrm{rpm}$.

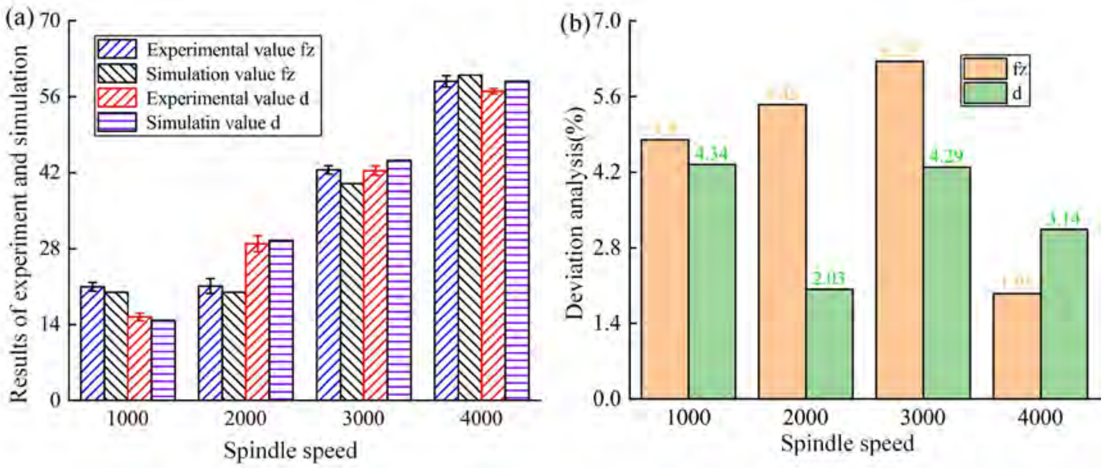

Figure 17. Comparisons between experimental and simulation results showing (a) the values of f_z and d obtained in experiment and simulation and (b) deviation analysis in (a).

5.3 Analysis of surface micro-hardness in CM and LTUAM

Surface micro-hardness is an important indicator for evaluating surface hardening and the plastic deformation of the sub-surface layer is the main reason for work hardening, which increases the strength and hardness of the surface material as reported in [63]. In addition, the improvement of surface micro hardness reduces the magnitude of deformation induced by alternating loads, prevents fatigue-related crack growth and improves fatigue performance. It can also help improve the wear resistance of components. During milling, the surface and subsurface materials undergo severe plastic deformation due to the strain hardening. Therefore, the microhardness of the machined surface is usually higher than that of the bulk material e.g. see [18].

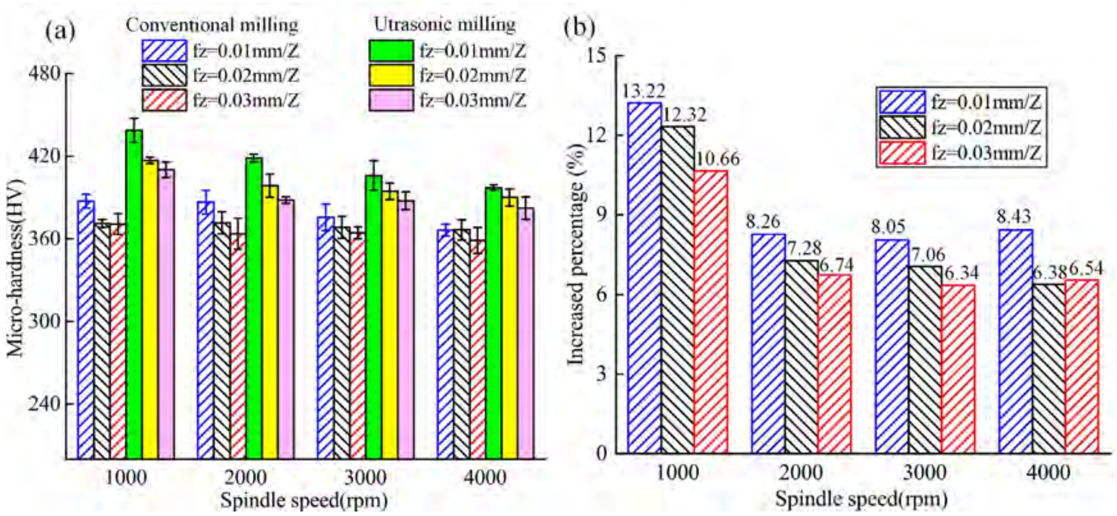

Figure 18. Influence of CM and RUEM on surface micro-hardness showing (a) micro-hardness value and (b) increased percentage between CM and LTUAM in (a).

Surface micro hardness values of both CM and LTUAM under different spindle speed and processing methods are measured as illustrated in Fig. 18. It can be noted that surface micro hardness values in LTUAM are enhanced between 6.34% and 13.22% compared with CM. Besides, lower spindle speeds and smaller feed speeds correspond to higher micro-hardness values. Specifically, maximum surface hardness value 438.61HV can be obtained when the feed per tooth is $0.1\,\mathrm{mm/Z}$ and spindle speed is $1000\mathrm{rpm}$ in LTUAM. This could be related with the deformation layer thickness of the sub-surface layer. Zhang *et al.* [41] observed a thicker subsurface deformation of Ti-4Al-6V at low cutting speed with rotary ultrasonic elliptical end milling. In addition, the machined surface is further strengthened due to the effect of ultrasonic vibration, which is similar to the mechanism of ultrasonic shot peening e.g. see [64]. It was reported that finer grains and nanocrystalline layers in the subsurface layer were found in ultrasonic machining as explained in [18,65], which could be primary reason of increased hardness in LTUAM.

6. Conclusions

In this work, machining characteristics including material removal kinematic process and ultrasonic surface generation of LTUAM are modelled and experimentally verified. The contact and separation behavior between the tool and workpiece in each ultrasonic cycle are understood through an analytical model. In order to analyze the generation of micro dimple textures, substantial numerical simulations are conducted using the developed simulation method. The effects of machining and ultrasonic parameters on the micro dimpled structures are evaluated quantitatively and the main conclusions are presented below.

The material removal process between tool and workpiece in LTUAM are studied analytically. The analysis of tool workpiece contact rate r demonstrates that the spindle speed is positively correlated with r, and ultrasonic frequency and the helix angle of the tool are negatively correlated with the r. Moreover, when vibration amplitudes are small, the contact rate r maintains 1 and as vibration amplitudes are increased, the contact rate r becomes lower.

An analytical surface topography model of LTUAM is firstly established. Furthermore, the influence of 3D tool topography is investigated for the analysis of the formation of micro dimpled surfaces. Different types of surface topography are simulated and it was found that the clearance angle and the secondary cutting edge of the tool were essential to understand the generation of micro dimples structures.

The effects of process parameters including spindle speed, feed per tooth, ultrasonic frequency) on the micro dimpled surface are discussed. The distance of micro dimpled surfaces increases with the improvement of the spindle speed and the reduction of the ultrasonic frequency. The position and arrangement of the micro dimpled textures can be controlled by changing the values of the parameters λ_1 and λ_2. Compared with CM, the obvious reduction of the cutting force was observed in LTUAM. This can be attributed to the high frequency intermittent cutting mechanism due to the application of ultrasonic vibration. It can be concluded ultrasonic vibration can change from continuous to discontinuous cutting.

The micro hardness test results confirmed that LTUAM significantly enhanced the surface micro hardness from 6.34% to 13.22% and the improvement of the surface micro hardness are decreased as the spindle speed is improved. In addition, maximum surface micro-hardness value 438.61HV can be obtained in LTUAM at $n = 1000\text{rpm}$.

Acknowledgments

This work was supported by the National Natural Science Foundation of China [51975112].

References

[1] Ni C, Zhu L, Yang Z. Comparative investigation of tool wear mechanism and corresponding machined surface characterization in feed-direction ultrasonic vibration assisted milling of Ti–6Al–4V from dynamic view. Wear, 2019, 436-437.

[2] Yang Z, Zhu L, Wang S, et al. Effects of ultrasound on multilayer forming mechanism of Inconel 718 in directed energy deposition. Additive Manufacturing, 2021, 48.

[3] Xue P, Zhu L, Xu P, et al. CrCoNi medium-entropy alloy thin-walled parts manufactured by laser metal deposition: Microstructure evolution and mechanical anisotropy. Materials Science and Engineering: A, 2021, 817.

[4] Zhang J, Cui T, Ge C, et al. Review of micro/nano machining by utilizing elliptical vibration cutting. International Journal of Machine Tools and Manufacture, 2016, 106: 109-126.

[5] Gao G, Xia Z, Su T, et al. Cutting force model of longitudinal-torsional ultrasonic-assisted milling Ti-6Al-4V based on tool flank wear. Journal of Materials Processing Technology, 2021, 291.

[6] Verma G C, Pandey P M, Dixit U S. Modeling of static machining force in axial ultrasonic-vibration assisted milling considering acoustic softening. International Journal of Mechanical Sciences, 2018, 136: 1-16.

[7] Yang Z, Zhu L, Zhang G, et al. Review of ultrasonic vibration-assisted machining in advanced materials. International Journal of Machine Tools and Manufacture, 2020, 156.

[8] Moriwaki T, Shamoto E. Ultraprecision Diamond Turning of Stainless Steel by Applying Ultrasonic Vibration. CIRP Annals, 1991, 40 (1): 559-562.

[9] Liu X, Zhang J, Hu X, et al. Influence of tool material and geometry on micro-textured surface in radial ultrasonic vibration-assisted turning. International Journal of Mechanical Sciences, 2019, 152: 545-557.

[10] Shen X-H, Zhang J-H, Li H, et al. Ultrasonic vibration-assisted milling of aluminum alloy. The International Journal of Advanced Manufacturing Technology, 2012, 63 (1-4): 41-49.

[11] Chen W, Zheng L, Xie W, et al. Modelling and experimental investigation on textured surface generation in vibration-assisted micro-milling. Journal of Materials Processing Technology, 2019, 266: 339-350.

[12] Wang H, Pei Z J, Cong W. A feeding-directional cutting force model for end surface grinding of CFRP composites using rotary ultrasonic machining with elliptical ultrasonic vibration. International Journal of Machine Tools and Manufacture, 2020, 152.

[13] Jiang J, Sun S, Wang D, et al. Surface texture formation mechanism based on the ultrasonic vibration-assisted grinding process. International Journal of Machine Tools and Manufacture, 2020, 156.

[14] Chen G, Zou Y, Qin X, et al. Geometrical texture and surface integrity in helical milling and ultrasonic vibration helical milling of Ti-6Al-4V alloy. Journal of Materials Processing Technology, 2020, 278.

[15] Wang J, Feng P, Zhang J, et al. Reducing cutting force in rotary ultrasonic drilling of ceramic matrix composites with longitudinal-torsional coupled vibration. Manufacturing Letters, 2018, 18: 1-5.

[16] Zhang T, Wang Z, Yu T, et al. Modeling and prediction of generated local surface profile for ultrasonic vibration-assisted polishing of optical glass BK7. Journal of Materials Processing

Technology, 2021, 289.

[17] Guo P, Ehmann K F. An analysis of the surface generation mechanics of the elliptical vibration texturing process. International Journal of Machine Tools and Manufacture, 2013, 64: 85-95.

[18] Zhang M, Zhang D, Geng D, et al. Surface and sub-surface analysis of rotary ultrasonic elliptical end milling of Ti-6Al-4V. Materials & Design, 2020, 191.

[19] Yang Z, Zhu L, Ni C, et al. Investigation of surface topography formation mechanism based on abrasive-workpiece contact rate model in tangential ultrasonic vibration-assisted CBN grinding of ZrO2 ceramics. International Journal of Mechanical Sciences, 2019, 155: 66-82.

[20] Ma C, Shamoto E, Moriwaki T, et al. Study of machining accuracy in ultrasonic elliptical vibration cutting. International Journal of Machine Tools and Manufacture, 2004, 44 (12-13): 1305-1310.

[21] Jin X, Xie B. Experimental study on surface generation in vibration-assisted micro-milling of glass. The International Journal of Advanced Manufacturing Technology, 2015, 81 (1-4): 507-512.

[22] Yuan S, Guo X, Zhang S, et al. Influence mechanism of defects on the subsurface damage and structural evolution of diamond in CMP process. Applied Surface Science, 2021, 566.

[23] Ni C, Zhu L. Investigation on machining characteristics of TC4 alloy by simultaneous application of ultrasonic vibration assisted milling (UVAM) and economical-environmental MQL technology. Journal of Materials Processing Technology, 2020, 278.

[24] Ni C, Zhu L, Liu C, et al. Analytical modeling of tool-workpiece contact rate and experimental study in ultrasonic vibration-assisted milling of Ti–6Al–4V. International Journal of Mechanical Sciences, 2018, 142-143: 97-111.

[25] Li S, Zhang D, Liu C, et al. Influence of dynamic angles and cutting strain on chip morphology and cutting forces during titanium alloy Ti-6Al-4 V vibration-assisted drilling. Journal of Materials Processing Technology, 2021, 288.

[26] Chen J, Ming W, An Q, et al. Mechanism and feasibility of ultrasonic-assisted milling to improve the machined surface quality of 2D Cf/SiC composites. Ceramics International, 2020, 46 (10): 15122-15136.

[27] Ning F, Wang H, Cong W, et al. A mechanistic ultrasonic vibration amplitude model during rotary ultrasonic machining of CFRP composites. Ultrasonics, 2017, 76: 44-51.

[28] Nath C, Rahman M. Effect of machining parameters in ultrasonic vibration cutting. International Journal of Machine Tools and Manufacture, 2008, 48 (9): 965-974.

[29] Brehl D E, Dow T A. Review of vibration-assisted machining. Precision Engineering, 2008, 32 (3): 153-172.

[30] Feng Y, Hsu F-C, Lu Y-T, et al. Force prediction in ultrasonic vibration-assisted milling. Machining Science and Technology, 2020, 25 (2): 307-330.

[31] Feng Y, Hsu F C, Lu Y T, et al. Temperature prediction of ultrasonic vibration-assisted milling. Ultrasonics, 2020, 108: 106212.

[32] Feng Y, Hsu F-C, Lu Y-T, et al. Residual stress prediction in ultrasonic vibration–assisted milling. The International Journal of Advanced Manufacturing Technology, 2019, 104 (5-8): 2579-2592.

[33] Kapitaniak M, Vaziri V, Páez Chávez J, et al. Experimental studies of forward and backward whirls of drill-string. Mechanical Systems and Signal Processing, 2018, 100: 454-465.

[34] Liao M, Wiercigroch M, Sayah M, et al. Experimental verification of the percussive drilling model. Mechanical Systems and Signal Processing, 2021, 146.

[35] Börner R, Winkler S, Junge T, et al. Generation of functional surfaces by using a simulation tool for surface prediction and micro structuring of cold-working steel with ultrasonic vibration assisted face milling. Journal of Materials Processing Technology, 2018, 255: 749-759.

[36] Guo P, Ehmann K F. Development of a tertiary motion generator for elliptical vibration texturing. Precision Engineering, 2013, 37 (2): 364-371.

[37] Wang Q, Liang Z, Wang X, et al. Modelling and analysis of generation mechanism of micro-surface topography during elliptical ultrasonic assisted grinding. Journal of Materials Processing Technology, 2020, 279.

[38] Wang Q, Zhao W, Liang Z, et al. Investigation of diamond wheel topography in Elliptical Ultrasonic Assisted Grinding (EUAG) of monocrystal sapphire using fractal analysis method. Ultrasonics, 2018, 84: 87-95.

[39] Zhou W, Tang J, Chen H, et al. A comprehensive investigation of surface generation and material removal characteristics in ultrasonic vibration assisted grinding. International Journal of Mechanical Sciences, 2019, 156: 14-30.

[40] Peng Z, Zhang X, Zhang D. Effect of radial high-speed ultrasonic vibration cutting on machining performance during finish turning of hardened steel. Ultrasonics, 2020, 111: 106340.

[41] Zhang M, Zhang D, Geng D, et al. Effects of tool vibration on surface integrity in rotary ultrasonic elliptical end milling of Ti–6Al–4V. Journal of Alloys and Compounds, 2020, 821.

[42] Chen W Q, Zheng L, Huo D H, et al. Surface texture formation by non-resonant vibration assisted micro milling. Journal of Micromechanics and Microengineering, 2018, 28 (2).

[43] Shen X H, Shi Y L, Zhang J H, et al. Effect of process parameters on micro-textured surface generation in feed direction vibration assisted milling. International Journal of Mechanical Sciences, 2020, 167.

[44] Zhu L, Ni C, Yang Z, et al. Investigations of micro-textured surface generation mechanism and tribological properties in ultrasonic vibration-assisted milling of Ti–6Al–4V. Precision Engineering, 2019, 57: 229-243.

[45] Zhang R, Steinert P, Schubert A. Microstructuring of Surfaces by Two-stage Vibration-assisted Turning. Procedia CIRP, 2014, 14: 136-141.

[46] Xu S, Shimada K, Mizutani M, et al. Fabrication of hybrid micro/nano-textured surfaces using rotary ultrasonic machining with one-point diamond tool. International Journal of Machine Tools and Manufacture, 2014, 86: 12-17.

[47] Kurniawan R, Kiswanto G, Ko T J. Surface roughness of two-frequency elliptical vibration texturing (TFEVT) method for micro-dimple pattern process. International Journal of Machine Tools and Manufacture, 2017, 116: 77-95.

[48] Kurniawan R, Ko T J. Surface topography analysis in three-dimensional elliptical vibration texturing (3D-EVT). The International Journal of Advanced Manufacturing Technology, 2019, 102 (5-8): 1601-1621.

[49] Lotfi M, Sajjady S A, Amini S. Wettability analysis of titanium alloy in 3D elliptical ultrasonic assisted turning. International Journal of Lightweight Materials and Manufacture, 2019, 2 (3): 235-240.

[50] Lu H, Zhu L, Yang Z, et al. Research on the generation mechanism and interference of surface texture in ultrasonic vibration assisted milling. International Journal of Mechanical Sciences, 2021, 208.

[51] Yang Z, Zhu L, Lin B, et al. The grinding force modeling and experimental study of ZrO2 ceramic materials in ultrasonic vibration assisted grinding. Ceramics International, 2019, 45 (7): 8873-8889.

[52] Yan Y, Xu J, Wiercigroch M. Non-linear analysis and quench control of chatter in plunge grinding. International Journal of Non-Linear Mechanics, 2015, 70: 134-144.

[53] Feng Y, Hsu F-C, Lu Y-T, et al. Surface roughness prediction in ultrasonic vibration-assisted milling. Journal of Advanced Mechanical Design, Systems, and Manufacturing, 2020, 14 (4): JAMDSM0063-JAMDSM0063.

[54] Feng Y, Hsu F-C, Lu Y-T, et al. Tool wear rate prediction in ultrasonic vibration-assisted milling. Machining Science and Technology, 2020, 24 (5): 758-780.

[55] Chen G, Ren C, Zou Y, et al. Mechanism for material removal in ultrasonic vibration helical milling of Ti 6Al 4V alloy. International Journal of Machine Tools and Manufacture, 2019, 138: 1-13.

[56] Wu C, Chen S, Xiao C, et al. Longitudinal–torsional ultrasonic vibration-assisted side milling process. Proceedings of the Institution of Mechanical Engineers, Part C: Journal of Mechanical Engineering Science, 2019, 233 (10): 3356-3363.

[57] Buj-Corral I, Vivancos-Calvet J, Domínguez-Fernández A. Surface topography in ball-end milling processes as a function of feed per tooth and radial depth of cut. International Journal of Machine Tools and Manufacture, 2012, 53 (1): 151-159.

[58] Zhou W, Tang J, Shao W. Modelling of surface texture and parameters matching considering the interaction of multiple rotation cycles in ultrasonic assisted grinding. International Journal of Mechanical Sciences, 2020, 166.

[59] Elhami S, Razfar M R, Farahnakian M. Analytical, numerical and experimental study of cutting force during thermally enhanced ultrasonic assisted milling of hardened AISI 4140. International Journal of Mechanical Sciences, 2015, 103: 158-171.

[60] Moriwaki T, Shamoto E. Ultrasonic Elliptical Vibration Cutting. CIRP Annals, 1995, 44 (1): 31-34.

[61] Amini S, Hosseinabadi H N, Sajjady S A. Experimental study on effect of micro textured surfaces generated by ultrasonic vibration assisted face turning on friction and wear performance. Applied Surface Science, 2016, 390: 633-648.

[62] Liu X, Wu D, Zhang J. Fabrication of micro-textured surface using feed-direction ultrasonic vibration-assisted turning. The International Journal of Advanced Manufacturing Technology, 2018, 97 (9-12): 3849-3857.

[63] Liu J, Jiang X, Han X, et al. Effects of rotary ultrasonic elliptical machining for side milling on the surface integrity of Ti-6Al-4V. The International Journal of Advanced Manufacturing Technology, 2018, 101 (5-8): 1451-1465.

[64] Sun Q, Han Q, Xu R, et al. Localized corrosion behaviour of AA7150 after ultrasonic shot peening: Corrosion depth vs. impact energy. Corrosion Science, 2018, 130: 218-230.

[65] Lotfi M, Amini S, Akbari J. Surface integrity and microstructure changes in 3D elliptical ultrasonic assisted turning of Ti–6Al–4V: FEM and experimental examination. Tribology International, 2020, 151.